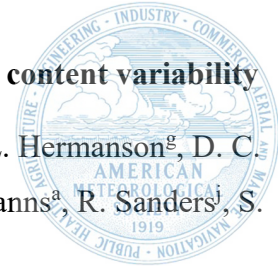


Ocean Heat Convergence and North Atlantic multidecadal heat content variability

B. I. Moat^a, B. Sinha^a, D. I. Berry^b, S. S. Drijfhout^{c, d, e}, N. Fraser^f, L. Hermanson^g, D. C. Jones^h, S. A. Josey^a, B. King^a, C. Macintoshⁱ, A. Megann^a, M. Oltmanns^a, R. Sanders^j, S. Williams^a



^a*National Oceanography Centre, Southampton, UK*

^b*WMO, Geneva, Switzerland*

^c*Royal Netherlands Meteorological Institute (KNMI), De Bilt, Netherlands*

^d*Ocean and Earth Science, University of Southampton, Southampton, UK*

^e*Faculty of Science, Utrecht University, Utrecht, Netherlands*

^f*Scottish Association for Marine Science, Scotland, UK*

^g*Met Office, Exeter, UK,*

^h*British Antarctic Survey, NERC, UKRI,, Cambridge, UK*

ⁱ*ESA Climate Office*

^j*NORCE, Norwegian Research Centre & Bjerknes Centre for Climate Research, Bergen*

Corresponding author: Bengamin Moat, bim@noc.ac.uk

Early Online Release: This preliminary version has been accepted for publication in *Journal of Climate*, may be fully cited, and has been assigned DOI 10.1175/JCLI-D-23-0370.1. The final typeset copyedited article will replace the EOR at the above DOI when it is published.

© 2024 The Author(s). Published by the American Meteorological Society. This is an Author Accepted Manuscript distributed under the terms of the Creative Commons Attribution 4.0 International (CC BY 4.0)

ABSTRACT

We construct an upper ocean (0-1000m) North Atlantic heat budget (26°-67°N) for the period 1950-2020 using multiple observational datasets and an eddy-permitting global ocean model. On multidecadal timescales ocean heat transport convergence controls ocean heat content (OHC) tendency in most regions of the North Atlantic with little role for diffusive processes. In the subpolar North Atlantic (45°N-67°N) heat transport convergence is explained by geostrophic currents whereas ageostrophic currents make a significant contribution in the subtropics (26°N-45°N). The geostrophic contribution in all regions is dominated by anomalous advection across the time-mean temperature gradient although other processes make a significant contribution particularly in the subtropics. The timescale and spatial distribution of the anomalous geostrophic currents are consistent with a simple model of basin scale thermal Rossby waves propagating westwards/northwestwards in the subpolar gyre and multidecadal variations in regional OHC are explained by geostrophic currents periodically coming into alignment with the mean temperature gradient as the Rossby wave passes through. The global ocean model simulation shows that multidecadal variations in the Atlantic Meridional Overturning Circulation are synchronized with the ocean heat transport convergence consistent with modulation of the west-east pressure gradient by the propagating Rossby wave.

SIGNIFICANCE STATEMENT

The purpose of the work is to understand why the North Atlantic Ocean warms up and cools down on timescales of about forty years. The key finding is that the temperature fluctuations are caused by an oceanic wave pushing the ocean surface up and down and causing ocean currents to change direction, pushing heat into and out of different parts of the ocean and draw down or emit heat to the atmosphere. The findings matter because the warm and cool periods affect the climate of the countries surrounding the North Atlantic. Climate models need to account for this oceanic wave process to correctly predict how it will change in future and affect the large-scale climate in a warming world.

1. Introduction

There is currently an increasing interest in decadal climate prediction. The World Climate Research Programme (WCRP) has designated Near-Term Climate Prediction as one of its Grand Challenges and decadal prediction features prominently in its Lighthouse

Activity on Explaining and Predicting Earth System Change (WCRP, 2023a, b). One of the areas of the globe with large potential decadal predictability is the North Atlantic (Yeager and Robson, 2017) and clear decadal to multidecadal signals in multiple climate variables are seen there (Robson et al., 2018). Due to its long historical record, spatio-temporal coverage and resolution, sea-surface temperature (SST) is the defining variable for Atlantic Multidecadal Variability (AMV, Kushnir, 1994). Skilful decadal prediction of any one of a number of related climate variables, for example the North Atlantic Oscillation Index (NAO), the Atlantic Meridional Overturning Circulation (AMOC) or North Atlantic ocean heat content (OHC), would allow us to forecast climatic impacts of AMV (e.g. Enfield et al., 2001; Knight et al., 2006; Msadek and Frankignoul, 2009; Sutton and Dong, 2012; Sutton et al., 2018) in the adjacent countries in Europe, Africa and North America and would bring significant socioeconomic benefits.

To confidently predict AMV a decade or more ahead we need to understand the mechanism behind its decadal variability. Many modelling studies have proposed that the proximate driver of AMV is the AMOC (Robson et al., 2012; Zhang 2008; Zhang and Zhang, 2015, see Zhang, 2019 for a comprehensive review of the subject) and there is also some evidence of this from proxy observations (McCarthy et al., 2015). The AMOC in turn is proposed to be driven by the NAO through its impact on oceanic deep convection (Robson et al., 2016). The AMV has also been proposed to feedback on the NAO via its subpolar SST signature raising the possibility of a coupled multidecadal oscillation (e.g. Sutton et al., 2018). However other explanations of the AMV have been proposed. One suggests that the multidecadal oscillation is imposed on the ocean by atmospheric variability (Clement et al., 2015, but see Zhang et al., 2019 for a critique of this hypothesis), whilst another suggests that linked variability in both AMOC and AMV emerges as a result of an internal ocean mode of variability involving basin-scale “thermal” Rossby wave propagation across the subpolar gyre (Sévellec and Federov, 2013, 2015).

Volcanoes (Ottera et al., 2010; Swingdouw et al., 2015) and anthropogenic aerosols (Booth et al., 2012) have been suggested to drive AMV. Robson et al. (2022) show that aerosols can impact the AMOC by modifying turbulent heat loss (and hence deep convection) over the subpolar gyre – a consequence of changing air temperatures over the North American continent. However it is also possible that a specific external driver is not necessary as an existing mode of variability either coupled, ocean only or atmospheric could

be excited by a non-specific injection of energy such as atmospheric weather noise (Sévellec and Huck, 2015).

Another challenge has been the lack of agreement between models on the AMV characteristics and its mechanism (Drews and Greatbatch, 2017; Muir and Federov, 2017; Sévellec and Sinha, 2018; Sutton et al., 2018). Even simulations with the same model but different resolutions may give different results. For example, a recent study (Lai et al., 2022) finds that density anomalies generated in the Labrador Sea are the dominant influence on the ocean circulation variability associated with AMV at eddy permitting ocean resolution, but when a non-eddy permitting resolution is used, density anomalies generated in the Nordic Seas are more important.

Many authors have sought to understand the dynamic and thermodynamic drivers of subpolar SST using state estimates or observations (e.g. Buckley et al., 2014; Roberts et al., 2017, Josey and Sinha 2022). Although some progress has been made, this is complicated because the SST is related to the temperature of the surface mixed layer which varies in depth and whose heat budget is strongly influenced by entrainment. Some authors have compromised by taking the heat budget over a fixed climatological mixed layer depth at each location rather than the actual mixed layer depth (Buckley et al., 2014, Roberts et al., 2017) which reduces the link with the SST, others have compromised by using the actual mixed layer depth, but at the cost of using a simplified heat budget (Josey and Sinha, 2022). Additionally surface heat fluxes and ocean heat transport convergence are more finely balanced than for the heat content over a larger fixed depth hence very accurate data is needed to attribute the dominant process (Moat et al., 2019). Dynamical attribution to the large-scale ocean circulation, the AMOC for example, is also difficult as the ocean circulation typically extends over depth scales many times larger than typical mixed layer depths.

Here, our approach is to investigate the upper ocean heat content, as this is an integral part of AMV. While there have been many studies investigating the link between AMOC and AMV (e.g. Robson et al., 2012; Zhang, 2008; Zhang and Zhang, 2015) these and others have focussed on the link between the AMOC and the full depth meridional ocean heat transport. These valuable studies are therefore limited in what they say about how changes in the full depth meridional heat transport lead to changes in regional upper ocean heat content.

In particular, the processes leading to regional heat transport convergence have received little attention even though for the purposes of skilful prediction it is necessary to faithfully reproduce the regional and temporal variation of the ocean heat transport convergence. These processes are the focus of the present study. As organised changes of OHC over large areas are needed to affect the overlying atmospheric circulation (the Jet Stream and the storm track), we focus on the North Atlantic Ocean heat budget over large spatial scales (1000+ km). We also choose a depth horizon of 1000 m (Buckley and Marshall, 2016; Hirschi et al., 2020; Moat et al., 2019).

We address the following questions:

1. What is the relative importance of ocean versus atmosphere processes in driving upper ocean heat content variability on multidecadal timescales?
2. Are changes in velocity, changes in temperature gradient or both important in determining the heat transport convergence and what controls these changes?
3. How does ocean heat transport convergence relate to the AMOC?

The paper is organised as follows: In Section 2, we describe data sources, ocean-ice model setup and our ocean heat budget decomposition. In Section 3, we present our results and Section 4 concludes with a summary and discussion.

2. Data and Methods

a. Datasets

OHC was derived from gridded temperature-salinity datasets: EN4.2.2 (Good et al. 2013); MOSORA (Smith et al., 2007; Smith et al., 2015); NOC Argo OI (Moat et al., 2021). SST and air-sea fluxes are obtained from the widely used ERA5 reanalysis (Hersbach et al., 2020). The OHC was estimated as the product of the volume, potential temperature, density (1000 kg m^{-3}) and specific heat capacity ($4200 \text{ J Kg}^{-1} \text{ K}^{-1}$). The data set resolutions are detailed in Table 1. Absolute surface geostrophic currents based on satellite altimetry were obtained from the Copernicus Climate Change Service Climate Data Store (2018). The vDT2021 data product used was used.

	spatial resolution	vertical resolution	temporal resolution
EN4.2.2	1°x1°	42 levels	monthly
MOSORA	1.25°x1.25°	20 levels	monthly
ArgoOI (surface to 2000m)	1°x1°	100 levels	10 day resolution averaged to monthly

Table 1. The gridded temperature-salinity datasets.

We use the NEMO ocean general circulation model (Madec et al., 2016) coupled to the CICE sea-ice model (Hunke et al., 1997) in the GO6 configuration (Storkey et al., 2018), which has a nominal resolution of $\sim 0.25^\circ$ and 75 vertical levels, to estimate the importance of ageostrophic effects. The model is forced by surface meteorological conditions using the CORE2 surface forcing dataset: 6-hourly 2m air temperature and humidity and 10m wind speed are used to calculate turbulent heat flux and surface wind stress. In addition, daily surface downwelling shortwave and longwave radiation, and monthly precipitation are prescribed by CORE2. Temperature and salinity are initialised using a climatology for 2004-2008 derived from EN4. The simulation covers 1948-2009 using the OMIP2 protocol (Tsuji no et al., 2020; Griffies et al., 2016), where the model starts with zero velocity and runs through five passes of the same forcing with the end state after each pass becoming the initial state of the next pass. We analyze output from the final pass.

b. Method

To account for different dynamical regimes (after Moat et al., 2019), we divide the North Atlantic into four subregions, subpolar west, subpolar east, subtropical west, subtropical east (Table 2, Fig. 2). We choose large regions because impacts on the atmospheric circulation require coherent anomalies over large length scales (Gastineau et al., 2015).

	Longitude range	Latitude range
Subpolar west	80°W-41°W	45°N-67°N
Subpolar east	41°W-0°E	45°N-67°N
Subtropical west	80°W-41°W	26°N-45°N
Subtropical east	41°W-0°E	26°N-45°N

Table 2. Definition of North Atlantic subregions regions.

We decompose the upper ocean heat budget beginning with the equation for potential temperature, $\theta(x, y, z, t)$, in local Cartesian coordinates, where x, y, z are zonal, meridional and depth coordinates and t is time:

$$\frac{\partial \theta}{\partial t} = -v \cdot \nabla \theta + \frac{\partial F}{\partial z} \quad (1)$$

v is the 3D ocean velocity, ∇ is the 3D gradient operator and F is vertical diffusive heat flux. We assume horizontal diffusion to be negligible.

Average (1) from surface to depth H :

$$\frac{\partial [\theta]}{\partial t} = \frac{Q_{net}}{\rho C_p H} - [v] \cdot \nabla [\theta] - [v^* \cdot \nabla \theta^*] + \frac{F_{-H}}{H} \quad (2)$$

where Q_{net} is the net surface heat flux, ρ is the density and C_p is the specific heat capacity. Square brackets indicate a depth average (0 to 1000m), variables with a * (asterisk) superscript represent a deviation from the depth average, $a = [a] + a^*$, $[a] = (\int_{-H}^0 a dz) / H$

The first term on the RHS of (2) represents atmospheric forcing whilst the other three terms represent ocean processes. We refer to the sum of these latter three terms on the RHS of (2) as the ocean heat supply. The ocean heat convergence is the sum of terms 2 and 3 on the RHS of (2).

Next, we decompose $[v]$ and $[\theta]$ into time averaged and time varying quantities where an overbar represents a long term time average and dashed variables are deviations from the time average, $a = \underline{a} + a'$, $\underline{a} = (\int_{T_1}^{T_2} a dt) / (T_2 - T_1)$:

$$\begin{aligned} \frac{\partial [\theta]'}{\partial t} = & \frac{Q'_{net}}{\rho C_p} - \overline{[v]} \cdot \nabla [\theta]' - [v]' \cdot \nabla \overline{[\theta]} - ([v]' \cdot \nabla [\theta]' - \overline{[v]' \cdot \nabla [\theta]'}) \\ & - [v^* \cdot \nabla \theta^*]' + F'_{-H} \end{aligned} \quad (3)$$

Finally, we perform a 2D spatial average represented by angled brackets, $\langle a \rangle = (\int_{y_1}^{y_2} \int_{x_1}^{x_2} a dx dy) / \{(y_2 - y_1)(x_2 - x_1)\}$.

$$\begin{aligned} \frac{\partial \langle [\theta]' \rangle}{\partial t} = & \frac{\langle Q'_{net} \rangle}{\rho C_p} - \langle \overline{[v]} \cdot \nabla [\theta]' \rangle - \langle [v]' \cdot \nabla \overline{[\theta]} \rangle - (\langle [v]' \cdot \nabla [\theta]' \rangle \\ & - \langle \overline{[v]' \cdot \nabla [\theta]'} \rangle) - \langle [v^* \cdot \nabla \theta^*]' \rangle \\ & + \langle F'_{-H} \rangle \end{aligned} \quad (4)$$

The cross terms are expanded as follows where a double asterisk superscript (**) denotes a deviation from the spatial average:

$$\langle \overline{[v]} \cdot \nabla[\theta]' \rangle = \langle \overline{[v]} \rangle \cdot \langle \nabla[\theta]' \rangle + \langle \overline{[v]}^{**} \cdot \nabla[\theta]'^{**} \rangle \quad (5)$$

$$\langle [v]' \cdot \nabla\overline{[\theta]} \rangle = \langle [v]' \rangle \cdot \langle \nabla\overline{[\theta]} \rangle + \langle [v]'^{**} \cdot \nabla\overline{[\theta]}^{**} \rangle \quad (6)$$

The advective part of the anomalous ocean heat supply can thus be decomposed into six scalar products of a velocity with a temperature gradient. Five terms involve depth averaged currents and temperature gradients: $\langle \overline{[v]} \rangle \cdot \langle \nabla[\theta]' \rangle$ the time and spatial mean velocity paired with the spatial mean of the anomalous temperature gradient; $\langle \overline{[v]}^{**} \cdot \nabla[\theta]'^{**} \rangle$ the spatial covariance of the mean velocity paired with the anomalous temperature gradient; $\langle [v]' \rangle \cdot \langle \nabla\overline{[\theta]} \rangle$ the spatial mean of the anomalous velocity paired with the time and spatial mean temperature gradient.; $\langle [v]'^{**} \cdot \nabla\overline{[\theta]}^{**} \rangle$ the spatial covariance of the anomalous velocity paired with the mean temperature gradient; and ($\langle [v]' \cdot \nabla[\theta]' \rangle - \langle \overline{[v]}' \cdot \nabla\overline{[\theta]}' \rangle$) which is the spatial mean of the anomalous velocity paired with the anomalous temperature gradient. Finally, we obtain a contribution from the spatial average of deviations from the vertical average current and depth average (0 to 1000m) temperature gradient $\langle [v^* \cdot \nabla\theta^*]' \rangle$. Our decomposition is similar to that of Menary et al. (2015) but our method focuses on horizontal heat divergence rather than horizontal heat flux, as we find this aids physical interpretation of the results as will become clear later (Sections 3e-i). The meaning of the spatial correlation terms is somewhat distinct from the more familiar temporal correlations which can be ascribed to transient eddy and wave activity. The spatial correlations reflect spatially coherent changes in the basin scale circulation, an example being meandering major current systems such as the Gulf Stream or the North Atlantic Current. Section 3g contains further discussion on this point in the context of the Western Subpolar region.

To evaluate these terms using observations, we approximate the 3D velocity vector v with the 2D geostrophic velocity (u_g, v_g) referenced to a (temporally or spatially variable) level of no motion:

$$u_g = -\frac{1}{f} \frac{\partial \psi}{\partial y} \quad (7)$$

$$v_g = \frac{1}{f} \frac{\partial \psi}{\partial x} \quad (8)$$

The streamfunction ψ is given by:

$$\psi = \int_{p_0}^p \alpha dp' \quad (9)$$

where α is the specific volume anomaly (reciprocal of *in situ* seawater density minus the reciprocal of seawater density at standard temperature and salinity), p is the hydrostatic pressure and p_0 is the pressure at the level of no motion (Pond and Pickard, 1983). We take p_0 to be the pressure at 1000m, but investigate the uncertainty introduced by adopting a fixed reference level in Section 3d. All variables are filtered to retain periods of 10 years and longer using a Hanning filter.

When analyzing the ocean model simulation, we use the full 3D velocity but also use the 3D geostrophic velocity derived from the model temperature and salinity fields to assess the importance of ageostrophic motion which is missing from the observed estimates.

As we rely heavily in this paper on the gridded EN4 dataset, based on objective analysis of spatially and temporally inhomogeneous observations of profiles of *in situ* temperature and salinity, it is appropriate to provide an indication of the data coverage over the upper 1000m of our chosen spatial region of the North Atlantic (80°W-0°E, 26°-67°N, Table 2). We therefore plot the number of temperature-salinity profiles in the dataset within our region of interest which span a depth of at least 900m (Fig. 1). The spatial density of profiles ranges from relatively sparse (1950-60s) to very dense (2000-2010s). Over the whole North Atlantic region of our study, the number of profiles per 1x1 degree square rises from 2.9 in the 1950s to 67 in the 2010s. There are relatively few extended spatial regions (> 5x5 degrees) with no data at all. The western subpolar region has relatively sparse coverage south west of the southern tip of Greenland in the 1970s and rather sparse coverage in the central Labrador Sea in the 1980s. The other major area of sparse coverage is the central subtropical gyre (40-60W, 26-35N) in the 1980s and to a lesser extent in the 1950s and 1960s. We therefore flag those regions and periods as carrying the most uncertainty. We note however that the western boundary and the path of the North Atlantic Current are well covered in all decades.

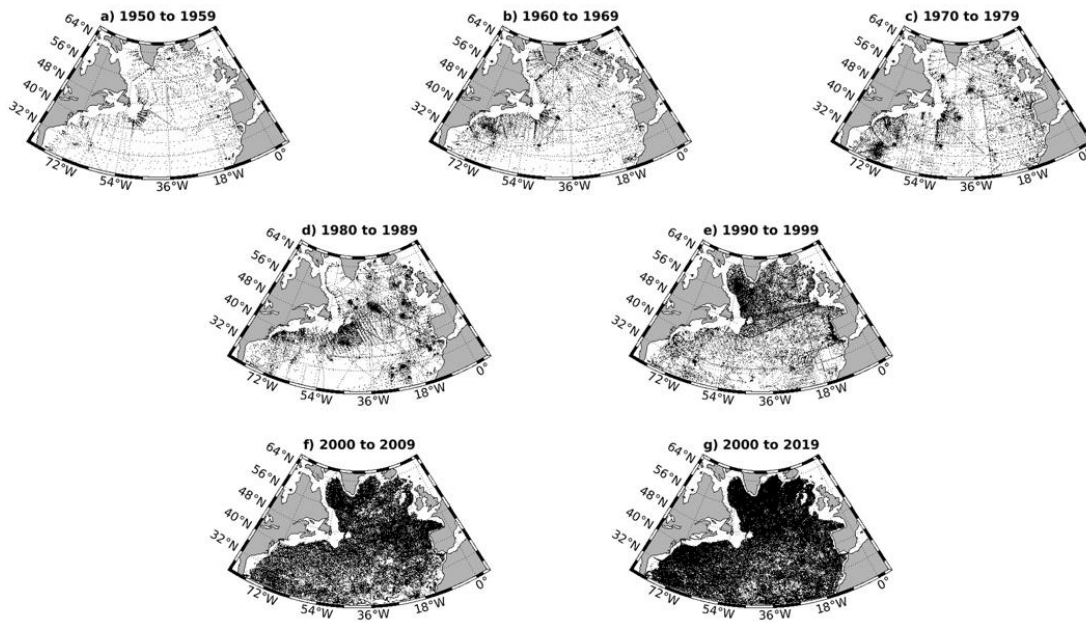


Fig 1. Locations of temperature-salinity depth profile observations going down to at least 900m below the surface per decade in the North Atlantic region of our study (80°W-0°E, 26°-67°N). Only profiles from the surface to 900m are shown. (a) 1950-1959 (b) 1960-1969) (c) 1970-1979 (d) 1980-1989 (e) 1990-1999 (f) 2000-2009 (g) 2010-2019.

3. Results

a. Heat content and AMV

We begin by exploring the relationship between upper ocean heat content and surface temperature, and how this varies spatially. Figure 2 shows simultaneous correlations of decadal filtered 0-1000 m OHC and SST over the period 1950-2020. Both time series were detrended and autocorrelations were considered in determining the degrees of freedom for significance testing (Emery and Thomson 1997). The variables are strongly positively correlated (r varies between 0.6 and 0.95) with significant correlation at the 95% level over the eastern subpolar North Atlantic and along the Gulf Stream path. However, correlations are weak ($r < 0.4$) south of about 30°N and anticorrelated close to the western boundary. The northwest corner (~40°W, 45°N) is also a region of anticorrelation. The relatively short timeseries and decadal filtering mean that the high correlations in the Labrador Sea are not significant at the 95% level, nonetheless the spatial coherence across the subpolar North Atlantic suggests a physical connection between OHC and SST across the whole region. We conclude that in the northern subtropics and in the subpolar regions decadal SST variability (and hence atmospheric impacts) covary strongly with 0-1000 m OHC. This motivates the

focus on OHC variability in this study i.e. if we can understand and predict the OHC, then since they covary, we can also predict the SST.

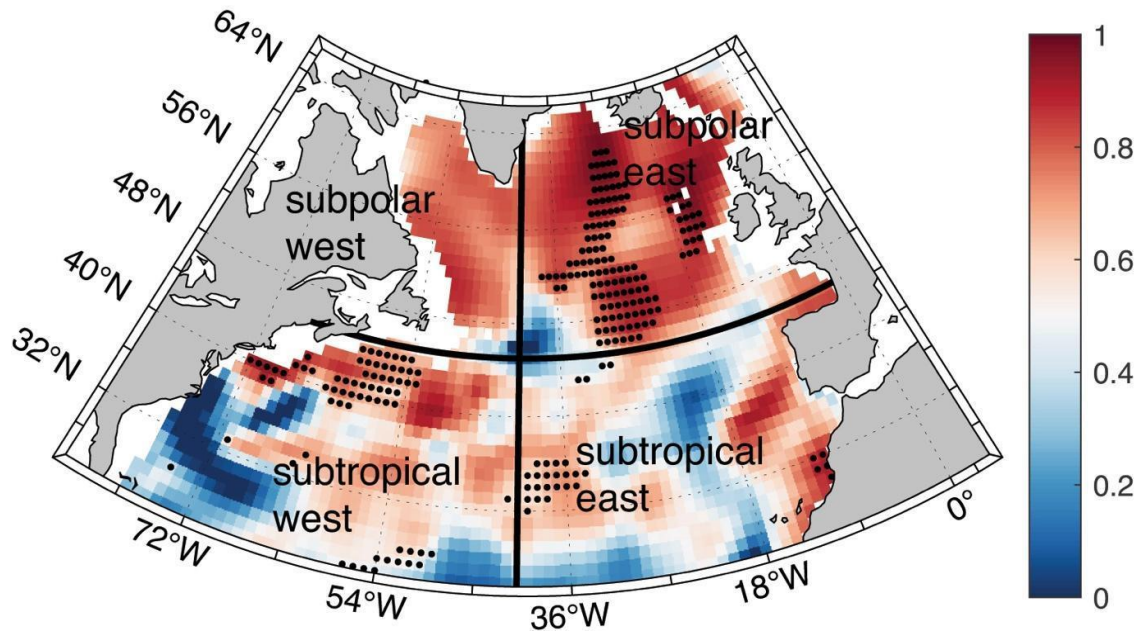


Fig. 2. Correlation coefficient between 0-1000m EN4 ocean heat content and EN4 sea surface temperature (SST). Both variables are 10 year lowpass filtered. Dots indicate values that are significant at the 95% level.

b. Ocean heat budget

The observation-based ocean heat budget over 1950-2020 in the four subregions is presented in Table 3. In Subpolar West, Subpolar East and Subtropical West, the mean surface heat flux is of order -40 W m^{-2} (negative sign implies heat loss from ocean to atmosphere) and ocean heat supply of order $+40 \text{ W m}^{-2}$ (positive implies convergence into the region) resulting in a small net OHC tendency. In Subtropical East, mean surface heat flux is positive and ocean heat supply is negative in contrast to the other regions and the mean magnitudes of the terms are much smaller, of order $+4 \text{ W m}^{-2}$. Interannual and decadal variability are larger in ocean heat supply than in surface heat flux.

	mean			interannual std deviation			decadal std deviation		
	Q _{net}	Ocean heat supply	Net OHC tendency	Q _{net}	Ocean heat supply	Net OHC tendency	Q _{net}	Ocean heat supply	Net OHC tendency
SPW	-42	42	0	13	19	15	4	5	4
SPE	-44	44	0	7	16	14	2	4	3
STW	-54	55	1	7	17	16	4	4	3
STE	4	-3	1	4	10	9	2	3	1

Table 3. Upper ocean (surface to 1000m) heat budgets for the North Atlantic subregions defined in Table 2. SPW=subpolar west, SPE=subpolar east, STW=subtropical east, STE=subtropical east. All values are in $W m^{-2}$. The interannual component is isolated by subtracting the decadal filtered variable from the unfiltered data.

Figure 3 shows the 1950-2020 decadal filtered heat budget (relative to 1981-2010) only including regions with water depth larger than 1000m. Net OHC tendency (brown) is a balance between anomalous surface heat flux (green) and ocean heat supply (blue). The OHC and surface flux terms are estimated independently, from ocean observations and atmospheric reanalysis respectively, whilst ocean heat supply is obtained as a residual of the other two terms. In all subregions, the three terms are of the order of several $W m^{-2}$. OHC tendency was obtained from three observational datasets (see Section 2a, datasets) and the brown shaded area provides an indication of the level of agreement between the datasets which is of order $1 W m^{-2}$. The ocean heat supply was also estimated based on the three different datasets (blue shaded area).

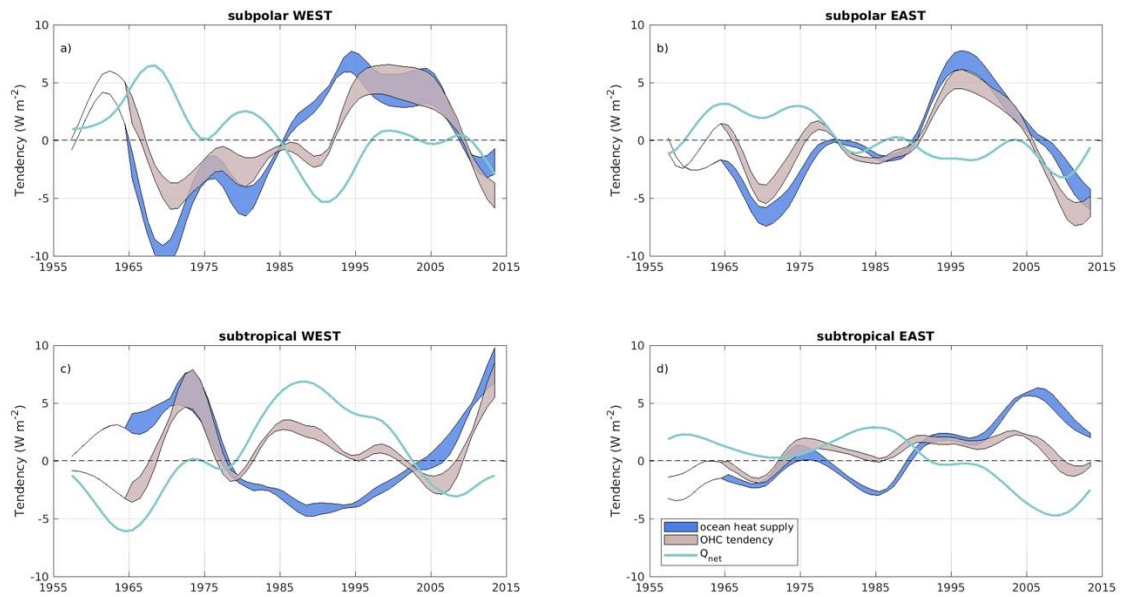


Fig. 3. Decadally filtered heat budget (0-1000m depth) from observations, 1950-2020, spatially averaged over a) subpolar west ($80^{\circ}\text{W}-41^{\circ}\text{W}$, $45^{\circ}\text{N}-67^{\circ}\text{N}$) b) subpolar east ($41^{\circ}\text{W}-0^{\circ}\text{E}$, $45^{\circ}\text{N}-67^{\circ}\text{N}$) c) subtropical west ($80^{\circ}\text{W}-41^{\circ}\text{W}$, $26^{\circ}\text{N}-45^{\circ}\text{N}$) d) subtropical east ($41^{\circ}\text{W}-0^{\circ}\text{E}$, $26^{\circ}\text{N}-45^{\circ}\text{N}$). Brown shading represents a range of estimates of ocean heat content tendency from three different datasets (EN4, ArgoOI and MOSORA), solid green line represents net surface heat flux anomaly (with respect to the full period) based on ERA5. Blue shading represents the ocean heat supply implied by the difference between the OHC tendencies and net surface heat flux. All heat budget terms are in W m^{-2} .

Multidecadal variability is present in all subregions. In Subpolar West, there is an alternation of positive and negative OHC tendency (Fig. 3a), with rapid declines in the 1960s and 2000s and a rising trend between the 1970s and 1990s. There is a long period from the mid 1960s to the mid 1980s and another from 1990 to 2015 where ocean heat supply dominates the ocean heat content trend. Subpolar East (Fig. 3b) displays similar behaviour with ocean heat supply dominating the OHC tendency even more strongly on decadal timescales and surface heat flux providing a damping. In particular, the warming in the 1990s and the cooling between 1965 and 1975 were driven by changes in ocean heat supply.

In Subtropical West (Fig. 3c), the terms tend to anticorrelate with the corresponding terms in Subpolar West, the most noteworthy difference being that the surface heat flux and ocean heat supply switch sign 5-10 years earlier in the subtropics (~ 1975 versus ~ 1985 and again ~ 2003 versus ~ 2010). There is a long period in between 1980 and 2000 where the surface heat flux drives the OHC tendency. Similarly, in Subtropical East (Fig. 3d) the ocean

heat supply is most often the same sign as the OHC tendency (hence the driving term) except for the period 1975-1990 when surface fluxes drive the net OHC tendency.

We next present (Fig. 4) a heat budget based on the NEMO ocean model (Section 2.2). The model OHC tendency variability over the North Atlantic is of similar magnitude to the observations ($\pm 4\text{--}5 \text{ W m}^{-2}$ in all four regions). However, there is much larger decadal variability in surface heat flux and ocean heat supply in the subpolar regions ($\pm 20 \text{ W m}^{-2}$ versus $\pm 10 \text{ W m}^{-2}$ in observations). In the subtropics, the decadal variability in heat flux and ocean heat supply is smaller than the observations ($\pm 6 \text{ W m}^{-2}$ versus $\pm 10 \text{ W m}^{-2}$ in the observations). Nonetheless, the evolution of the three terms in the model is similar to observations. In the subpolar regions, we have a rising trend in OHC tendency between the 1970s and 1990s and declining trends from the 1950s to about 1970 and again after 1992. The ocean heat flux (blue) is almost always the same sign as the heat content trend and hence the driving term, whereas the air-sea heat flux is of opposite sign, qualitatively similar to the observations. In Subtropical West, the peak in OHC tendency around 1972 (Fig. 4c) is well captured although the later rising trend appears too early, in the early 2000s in the model instead of the late 2000s in observations. In the eastern subtropics, the transition from a negative heat content trend to a positive trend around 1975 is captured by the model. Thus, the model provides a qualitatively plausible simulation of the North Atlantic upper ocean heat content.

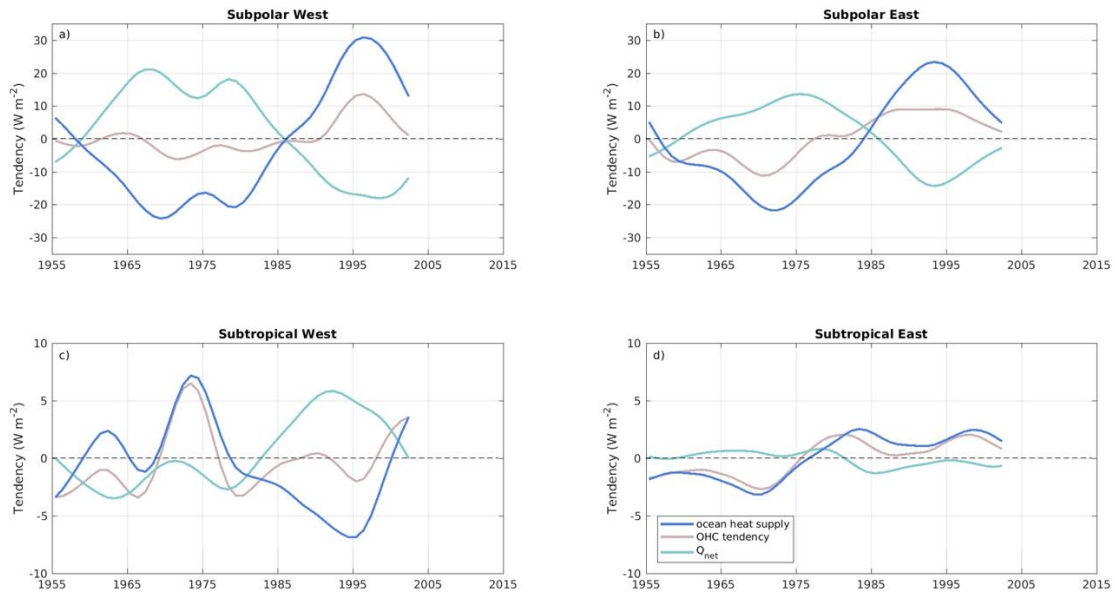


Fig. 4. Decadally filtered heat budget (0-1000m depth) from the NEMO ORCA025 OMIP2 forced ocean simulation, 1948-2009, spatially averaged over a) subpolar west (80°W - 41°W , 45°N - 67°N) b) subpolar east (41°W - 0°E , 45°N - 67°N) c) subtropical west (80°W - 41°W , 26°N - 45°N) d) subtropical east (41°W - 0°E , 26°N - 45°N). Ocean heat content (OHC) tendency (brown), net surface heat flux anomaly (green) and ocean heat supply (blue).

c. Importance of geostrophic and ageostrophic advection, and non-advective processes

Next, we examine the extent to which horizontal advection by the geostrophic flow accounts for the ocean heat supply on decadal timescales. Due to the high level of agreement between the gridded temperature-salinity datasets (Fig. 3), in this and subsequent analysis we will focus on just one representative dataset, EN4. We initially choose 1000m as a reference level for geostrophic calculations. In Fig. 5, the ocean heat supply (blue) is compared with an estimate of the horizontal heat convergence by geostrophic currents (red). There is good correspondence between the two in Subpolar East (Fig. 5b) but poor correspondence in the other three regions. In Subpolar West, the geostrophic heat convergence has a series of peaks and troughs (coinciding with periods of intensified Labrador Sea deep convection in the 1970s, 1990s, 2010s see Desbruyères et al., 2020) superimposed on a rising trend. In subtropical west the geostrophic convergence makes a large positive excursion around 1970 followed by a large negative excursion around 1995. Ocean heat convergence is anticorrelated with ocean heat supply in Subtropical East.

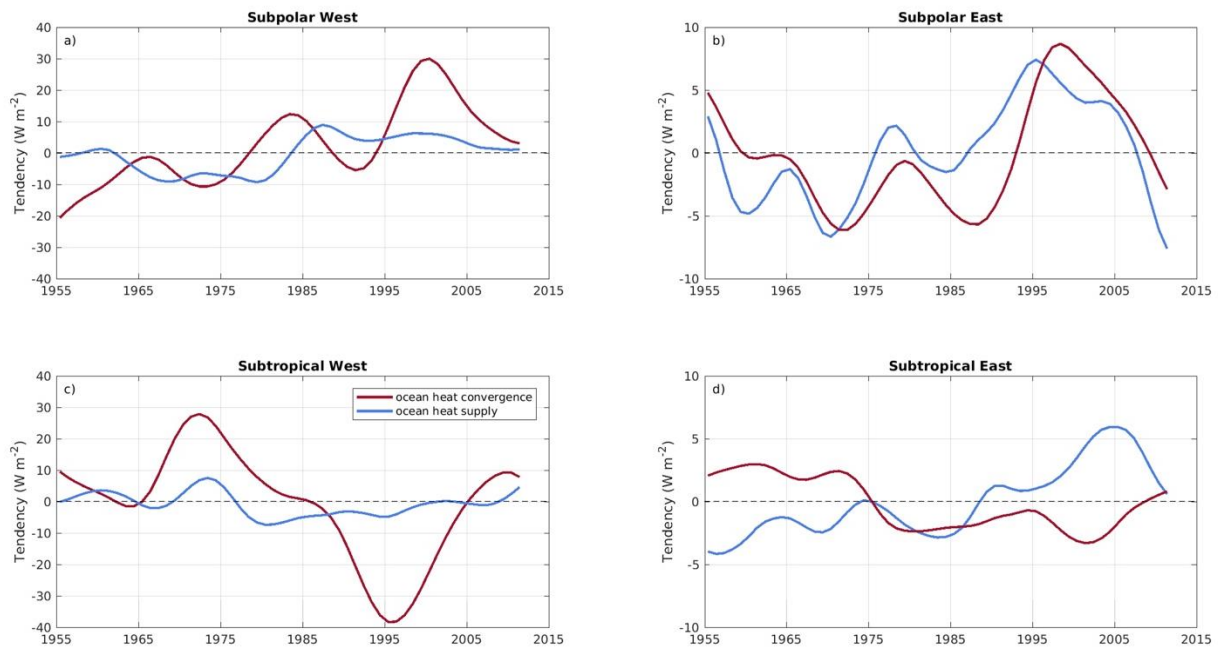


Fig. 5. Comparison of decadal filtered 0-1000m ocean heat supply ($W m^{-2}$), 1950-2020, obtained as a residual between ERA5 surface heat flux and EN4 0-1000m ocean heat content tendency (solid blue line) with decadal filtered 0-1000m ocean heat convergence based on geostrophic velocities referenced to 1000m depth calculated from EN4 (solid red) spatially averaged over a) subpolar west ($80^{\circ}W-41^{\circ}W$, $45^{\circ}N-67^{\circ}N$), b) subpolar east ($41^{\circ}W-0^{\circ}E$, $45^{\circ}N-67^{\circ}N$), c) subtropical west ($80^{\circ}W-41^{\circ}W$, $26^{\circ}N-45^{\circ}N$), d) subtropical east ($41^{\circ}W-0^{\circ}E$, $26^{\circ}N-45^{\circ}N$).

To understand the relationship between ocean heat convergence and ocean heat supply, we use our NEMO ocean model simulation (Fig. 6) to estimate the magnitude of ageostrophic advection which is difficult to obtain from observations. The model diagnostics allow us to calculate both the net and the geostrophic ocean heat convergences (red and black respectively) and compare with the ocean heat supply (blue). In all regions except Subpolar West, the net convergence (red) is very close to the ocean heat supply (blue). In Subpolar West, non advective processes (horizontal/vertical diffusion, entrainment/detrainment) contribute to ocean heat supply, but do not dominate. We also note that in both subpolar regions, the geostrophic heat convergence is very similar to the net convergence hence ageostrophic currents can be neglected in the heat budget. However, in the subtropical regions, the net and geostrophic convergences are substantially different, implying that ageostrophic currents are of direct importance to the multidecadal heat budget.

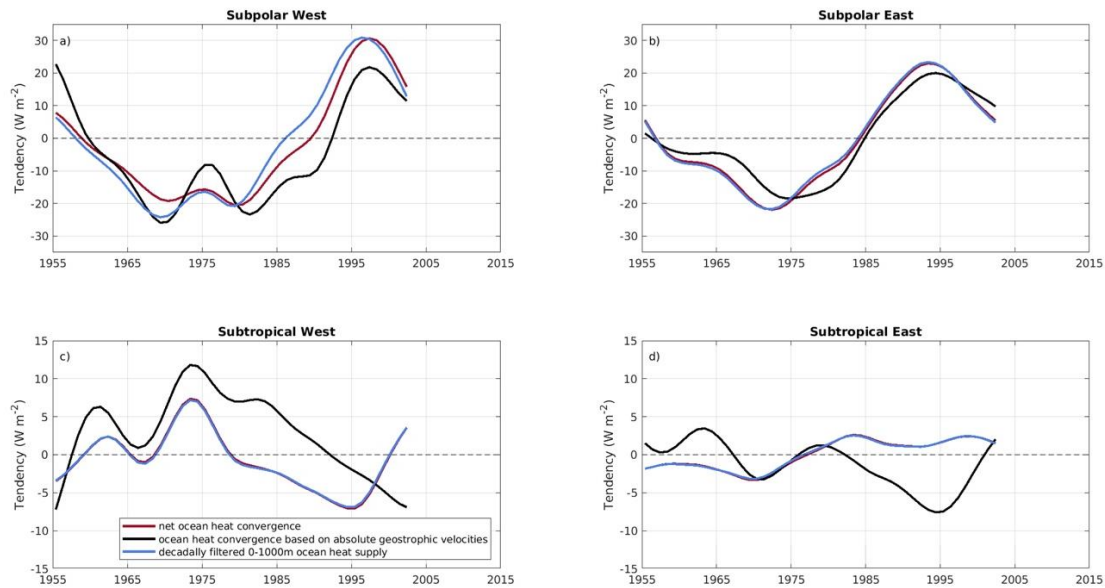


Fig. 6. Comparison of decadal filtered 0-1000m ocean heat supply (W m^{-2}), 1948-2009, obtained as a residual between surface heat flux and 0-1000m ocean heat content tendency (solid blue line) with decadal filtered ocean heat convergence based on absolute geostrophic velocities (solid black line), all from the NEMO ORCA025 OMIP2 forced ocean simulation, spatially averaged over a) subpolar west ($80^{\circ}\text{W}-41^{\circ}\text{W}$, $45^{\circ}\text{N}-67^{\circ}\text{N}$) b) subpolar east ($41^{\circ}\text{W}-0^{\circ}\text{E}$, $45^{\circ}\text{N}-67^{\circ}\text{N}$) c) subtropical west ($80^{\circ}\text{W}-41^{\circ}\text{W}$, $26^{\circ}\text{N}-45^{\circ}\text{N}$) d) subtropical east ($41^{\circ}\text{W}-0^{\circ}\text{E}$, $26^{\circ}\text{N}-45^{\circ}\text{N}$). Solid red line shows decadal filtered ocean heat convergence based on full 3D velocities.

d. Role of geostrophic reference level in explaining discrepancies between ocean heat supply and geostrophic heat convergence

If we accept the model evidence that ageostrophic currents are unimportant for the subpolar multidecadal heat budget, then the lack of correspondence between geostrophic heat convergence and ocean heat supply in Subpolar West (Fig. 5a) raises questions. In the subtropical regions, ageostrophic currents may explain the discrepancy between the ocean heat supply and the geostrophic convergence seen in Subtropical East (Figs. 5d versus 4d). However, in Subtropical West, the observations show an overly large geostrophic component in the 1990s (Fig. 5c versus 4c). These discrepancies suggest the assumption of a fixed 1000 m geostrophic reference level is questionable in the western subregions.

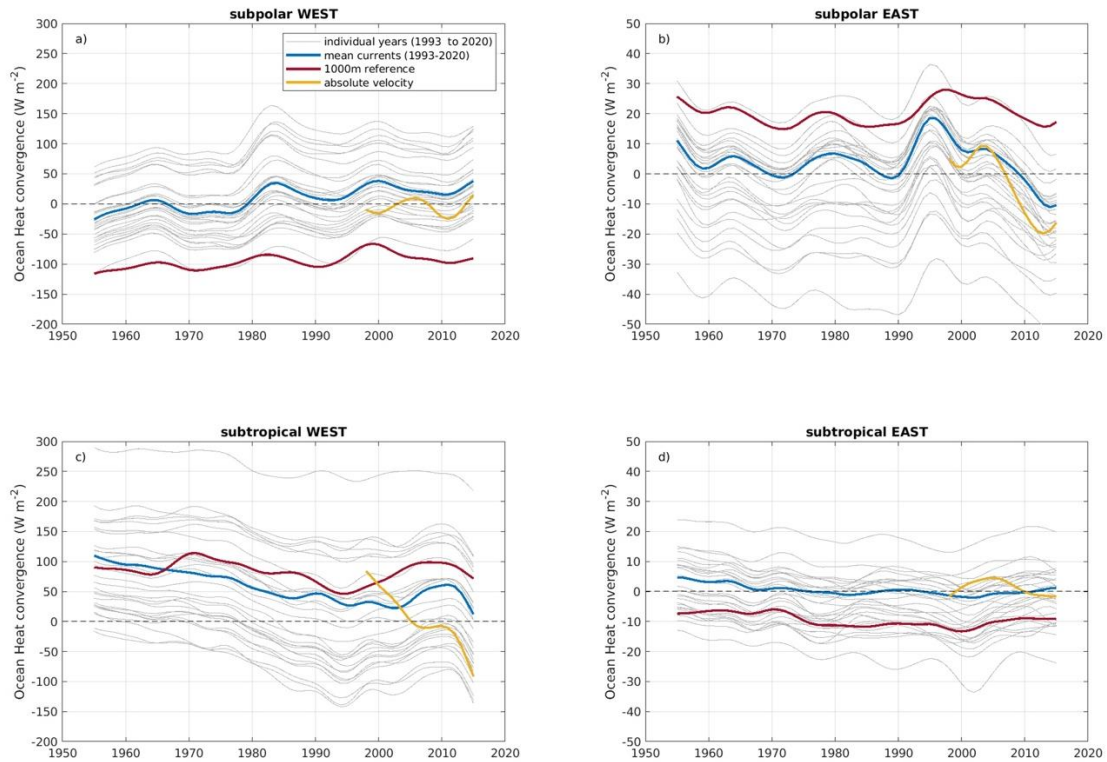


Fig. 7. Dependence of the ocean heat convergence on choice of reference level. Absolute geostrophic heat convergence for the period 1993-2020 using absolute surface geostrophic currents based on satellite altimetry (gold lines), surface currents for each individual year of the satellite period (1993 to 2020) as the reference velocity (grey lines), heat convergence based on a 1000m reference level (red) and average absolute surface currents from the satellite period (1993-2020) used to provide a reference velocity for the geostrophic calculations (blue line).

To follow up on this idea, we compare the geostrophic ocean heat convergence calculated using a reference level of 1000m (i.e. the red lines in Fig. 5) with the absolute geostrophic heat convergence for the period 1993-2020 using absolute geostrophic currents based on satellite altimetry as the reference velocity (i.e. using equation (9), but assuming that the geostrophic current is equal to satellite-based values at the surface, and then integrating downward to 1000m Fig. 7, gold lines). Note that both curves are anomalies from the 1993-2020 mean of the absolute heat convergence. As we are most interested in explaining the decadal variability, we can disregard the large mean offsets between the absolute geostrophic ocean heat convergence and the one based on a 1000m reference level (up to 100 W m^{-2} in the western subregions (Fig. 7a, c), but more like 20 W m^{-2} in the eastern subregions (Fig. 7b, d)). In Subtropical West (Fig. 7a) the heat convergence based on a 1000m reference level (red line) shows a decline of magnitude $\sim 20 \text{ W m}^{-2}$ from the year 2000 to 2012 followed by a slight upturn. In contrast the absolute heat convergence shows a decadal timescale variation of magnitude about 25 W m^{-2} . In Subpolar East, the 1000m based

heat convergence does capture a decline from the year 2000 onwards that is seen in the absolute heat convergence, but significantly underestimates the magnitude ($\sim 15 \text{ W m}^{-2}$ versus 20 W m^{-2}). In Subtropical West, the 1000m reference level is insufficient to capture the steep decline in the absolute heat convergence between 2000 and 2005, the plateau until 2010 and the subsequent further decline to the present. Finally in Subtropical East, the rising trend seen in the 1000m based estimate is not seen in the absolute heat convergence, which instead shows a decadal timescale increase and decrease. We next use the average absolute surface currents from the satellite period (1993-2020) to provide a temporally-unvarying reference velocity for the geostrophic calculations (blue line) and as a measure of uncertainty we also use the surface currents for each individual year of the satellite period (1993, 1994 etc to 2020) as a temporally-unvarying reference velocity (grey lines). In all subregions, the grey lines are generally strongly correlated with the blue line, suggesting that the temporal variation of the geostrophic heat convergence in these large regions does not depend very strongly on the choice of reference velocity/level. However only in the Subpolar East region do we get a good match between the blue line and the gold line. In Subpolar East therefore, using a mean surface reference velocity based on absolute satellite derived surface currents can be used to reconstruct the ocean heat convergence back to 1950. In contrast in the other three regions this is not possible and we require a temporally varying reference velocity to reproduce the absolute currents over the 1993-2020 period. Understanding how the reference velocity should change in earlier epochs is a non-trivial task and requires significant further research.

In summary, taking Figures 5 and 7 together, we can say that in Subtropical East, the ocean heat convergence based on a 1000m based reference level largely explains the ocean heat supply, although the amplitude of the variability is probably somewhat too small. In the other regions, the 1000m based ocean heat convergence explains a non-negligible part of the variability, but other processes related to a temporally changing reference velocity (equivalently changing level of no motion/barotropic velocity) make a significant contribution. In the subtropical regions ageostrophic heat convergence is likely to play a significant role.

e. Approximating geostrophic heat convergence using area and depth-averaged velocity and temperature gradients

Having established the importance of geostrophic ocean heat convergence, we next investigate whether temporal fluctuations in velocity or in temperature gradient dominate the

heat convergence, or if both processes contribute significantly and how much horizontal variations of velocity and temperature contribute. Figure 8 plots the geostrophic heat convergence (blue) over each region (based on a 1000m reference level) decomposed into six contributions (Section 2.2 equations (4)-(6)): $\langle \overline{[v]} \rangle \cdot \langle \nabla[\theta]' \rangle$, the time and spatial mean velocity paired with the spatial mean of the anomalous temperature gradient (solid black); $\langle \overline{[v]}^{**} \cdot \nabla[\theta]'^{**} \rangle$, the spatial covariance of the mean velocity paired with the anomalous temperature gradient (purple triangles); $\langle [v]' \rangle \cdot \langle \nabla\overline{[\theta]} \rangle$, the spatial mean of the anomalous velocity paired with the time and spatial mean temperature gradient (gold); $\langle [v]'^{**} \cdot \nabla\overline{[\theta]}'^{**} \rangle$, the spatial covariance of the anomalous velocity paired with the mean temperature gradient (light red squares); and $(\langle [v]' \cdot \nabla[\theta]' \rangle - \langle \overline{[v]}' \cdot \nabla\overline{[\theta]}' \rangle)$, the spatial mean of the anomalous velocity paired with the anomalous temperature gradient (dashed-dot dark red). Finally, we have a contribution from the spatial average of deviations from the depth average current and depth average temperature gradient $\langle [v]^* \cdot \nabla\theta^* \rangle'$ (dashed black).

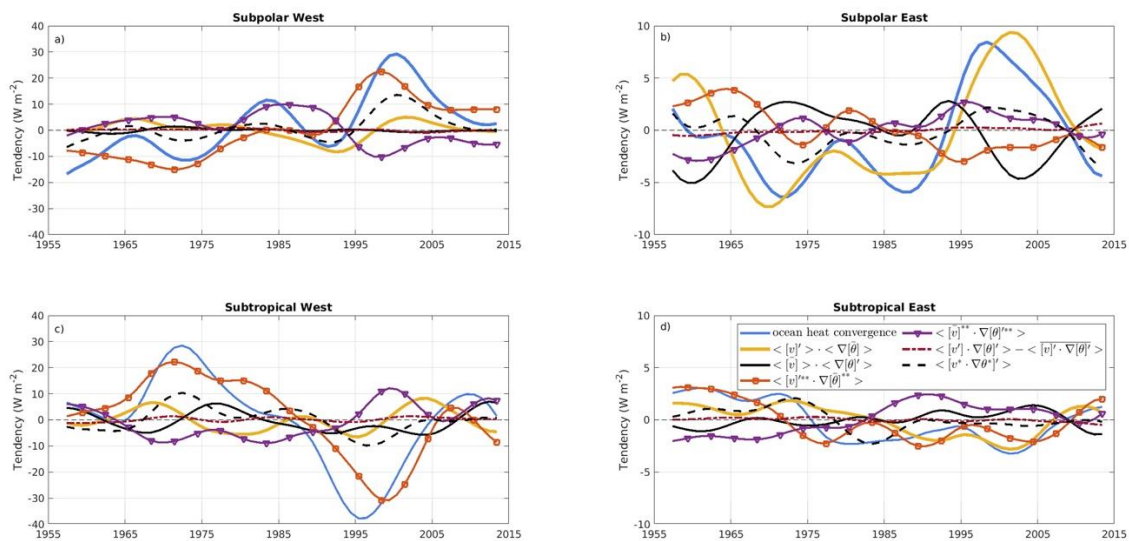


Fig. 8. Decomposition of the observed (EN4 dataset) decadal filtered 0-1000m ocean heat convergence based on geostrophic velocities, 1950-2020, spatially averaged over a) subpolar west (80°W-41°W, 45°N-67°N), b) subpolar east (41°W-0°E, 45°N-67°N), c) subtropical west (80°W-41°W, 26°N-45°N), d) subtropical east (41°W-0°E, 26°N-45°N). Blue – ocean heat convergence, solid black – spatially averaged time mean velocity acting on spatially averaged anomalous temperature gradient, dashed black – vertical covariance term, gold - spatially averaged anomalous velocity acting on spatially averaged time mean temperature gradient, dark red dashed-dotted – spatial average of anomalous velocity acting on anomalous temperature gradient, purple triangles – spatial covariance of time mean velocity acting on spatially averaged anomalous temperature gradient, red squares – spatial covariance of anomalous velocity acting on spatially averaged time mean temperature

gradient. All terms are in W m^{-2} . The reference level for geostrophic velocities is referenced to 1000m depth.

Recall that in Subtropical East, the geostrophic ocean heat convergence more or less explains the overall ocean heat supply. In this region (Fig. 8b), correlated variations of horizontal and vertical spatial anomalies in velocity fields and temperature gradients are of lesser importance and the ocean heat supply over the whole region is well characterised by using the spatially and depth averaged anomalous velocity and mean temperature gradient to determine the heat convergence (gold). This term is opposed by the spatially and depth averaged mean velocity acting on the anomalous temperature gradient (solid black) and reinforced by vertical fluctuations of velocity and temperature gradient (dashed black). The spatial correlation terms (purple triangles, light red circles) oppose each other and tend to cancel out. The least important term is the correlation between anomalous velocity and anomalous temperature gradient (dark red squares).

In Subpolar West (Fig 8a), correlated horizontal spatial variations of anomalous currents and the mean temperature gradient (light red circles) dominate the geostrophic ocean heat convergence (blue) and the corresponding spatial mean term (gold) is a relatively small term. The vertical correlation term (correlated vertical variations in the velocity field and the temperature gradient - dashed black) also plays a significant role, increasing with time and related to the decadal alternation between periods of Labrador Sea deep convection (Desbruyères et al., 2020). Horizontal spatial correlations of mean currents and anomalous temperature gradients (purple triangles) act in opposition to these terms.

In Subtropical West (Fig. 8c), the two horizontal correlation terms are again found to dominate. The horizontal correlations of the anomalous velocity and the mean temperature gradient (light red circles) explain most of the geostrophic ocean heat convergence and is opposed by horizontal correlations between the mean velocity and the anomalous temperature gradient (purple triangles).

Subtropical East (Fig 8d) presents a more complex picture with different terms important at different times. However, the terms involving anomalous velocity acting on mean temperature gradients (both spatial mean (gold) and correlations (light red circles)) and the vertical correlation term (dashed black) are the drivers. They are opposed by the terms involving the mean velocity acting on the anomalous temperature gradient (solid black and purple triangles).

f. The role of anomalous velocity in the temporal variations in geostrophic heat convergence.

Reverting to a 2D perspective (Fig. 9), we plot correlations between the net heat convergence term (excluding vertical correlations), $\overline{[v]} \cdot \nabla[\theta]' + [v]' \cdot \nabla\overline{[\theta]} + ([v]' \cdot \nabla[\theta]' - \overline{[v]}' \cdot \nabla[\theta]')$, and each of the components: anomalous current times mean temperature gradient ($[v]' \cdot \nabla\overline{[\theta]}$, Fig. 9a); mean current times anomalous temperature gradient ($\overline{[v]} \cdot \nabla[\theta]'$, Fig. 9b); and anomalous current times anomalous temperature gradient ($[v]' \cdot \nabla[\theta]' - \overline{[v]}' \cdot \nabla[\theta]'$), Fig. 9c). Figure 9a (anomalous current \times mean gradient) is dominated by positive correlations, and a large part of the variance in the ocean heat supply on decadal (and longer) timescales is caused by fluctuations in the current alone. Conversely, there are two elongated regions where the correlation is small/negative, and these seem to be associated with the Gulf Stream/North Atlantic Current and the subtropical return flow. Figure 9b, (mean current \times anomalous gradient), is predominantly small/negative and only positive in the regions with strong currents. This explains the balances over the wider areas in Fig. 8, in particular the general anticorrelation between the terms involving the anomalous velocity/mean temperature gradient versus those involving the mean velocity/anomalous temperature gradient. The correlation between the net convergence term and the anomalous velocity times anomalous temperature gradient is shown in Fig. 9c which reveals weak correlations and little coherence over large spatial scales compared to the other terms. Exceptions to this include the central Subpolar Gyre ($\sim 55\text{N}$, 36W) and the central Subtropical Gyre ($\sim 30\text{N}$, $40\text{-}60\text{W}$). The reasons for significant correlations in these regions are not immediately clear but may be related to eddy processes.

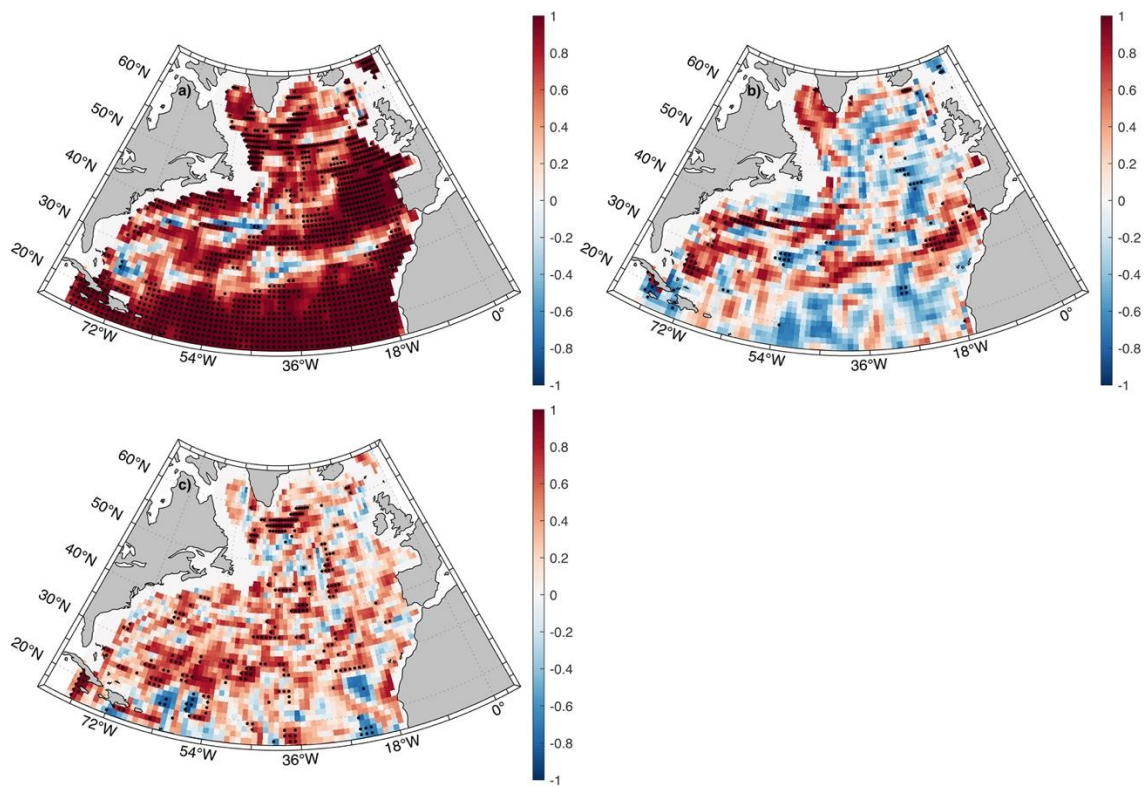


Fig. 9. Correlation between the observed (EN4 dataset, 1950 to 2020) decadal filtered 0-1000m ocean heat convergence based on geostrophic velocities and a) the component due to anomalous velocity acting on time mean temperature gradient b) the component due to time mean velocity acting on anomalous temperature gradient c) the component due to anomalous velocity acting on anomalous temperature gradient. Dots indicate values that are significant at the 95% level.

g. The role of anomalous geostrophic currents and the mean temperature gradient in determining the multidecadal variations in ocean heat convergence

Having established the importance of anomalous currents acting on the mean temperature gradient, we plot current vectors (blue) for every year in each subregion along with corresponding mean (negative) temperature gradient (red) vectors (Fig. 10). The key to understanding how these two vectors determine the ocean heat convergence (and hence ocean heat supply) is that the scalar product of two vectors depends on both the magnitudes of the vectors and the angle between them. Zero convergence occurs when the vectors are at right angles to each other (e.g. around 1994 and 2008 in the eastern subpolar region). Positive convergence generally occurs when the velocity is at an acute angle ($< 90^\circ$) to the mean temperature gradient (1960s, 1990s, 2000s) and negative convergence occurs when the angle is obtuse ($> 90^\circ$) (1970s, 1980s, 2010s). Extremes of ocean heat convergence occur when the two vectors are aligned (0° , e.g. 1997) or oppositely aligned (180° , e.g. 1988).

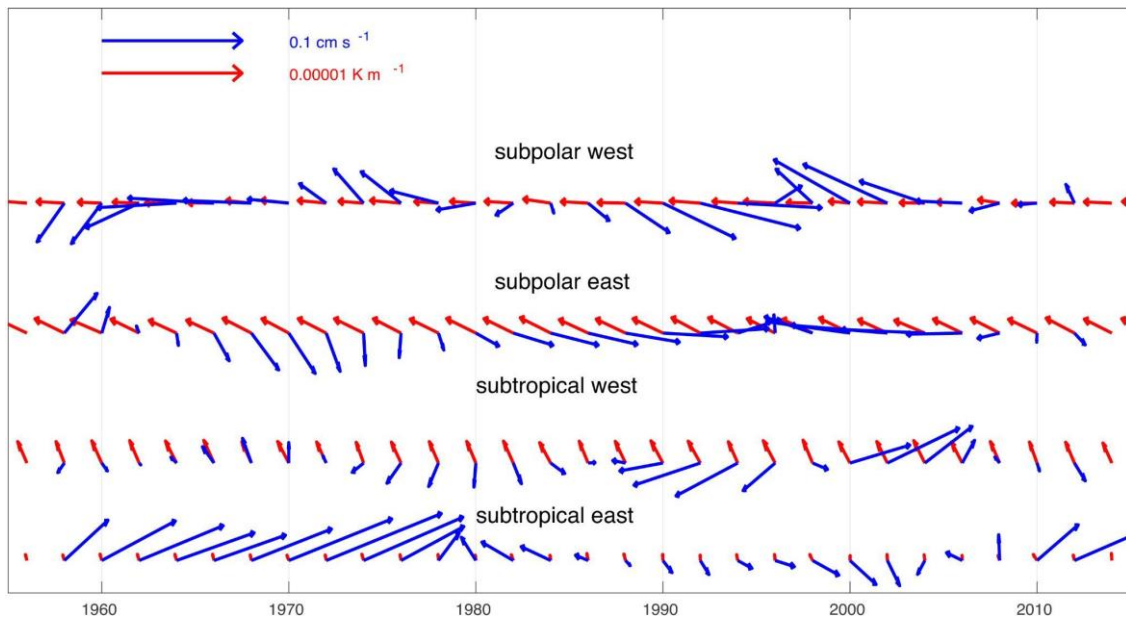


Fig. 10. Vectors of observed (EN4) decadal averaged, 0-1000m depth, anomalous geostrophic velocity (blue) and (negative) time mean temperature gradient (red) spatially averaged over subpolar west (80°W-41°W, 45°N-67°N); subpolar east (41°W-0°E, 45°N-67°N); subtropical west (80°W-41°W, 26°N-45°N); subtropical east (41°W-0°E, 26°N-45°N) for the period 1950-2020. The reference level for geostrophic velocities is referenced to 1000m depth.

The standout feature of the vector plots is the tendency of the velocity vector to rotate anticlockwise, seen for example in Subpolar East in the 1960s and 1990s, Subpolar West in the 1990s, in the Subtropical West around 1970 and again around 2010 (~10 year phase difference with the subpolar regions). In Subtropical East, the phenomenon occurs around 1977, a further ~7 year phase difference from the western subtropics. The periods with fast anticlockwise rotation are relatively short and alternate with periods of negative (southward directed) currents which gradually turn anticlockwise in the 1970s to early 1980s in Subpolar West, stretching into the 1990s in Subpolar East, the 1980s to early 1990s in Subtropical West and the 1990s to 2000s in Subtropical East.

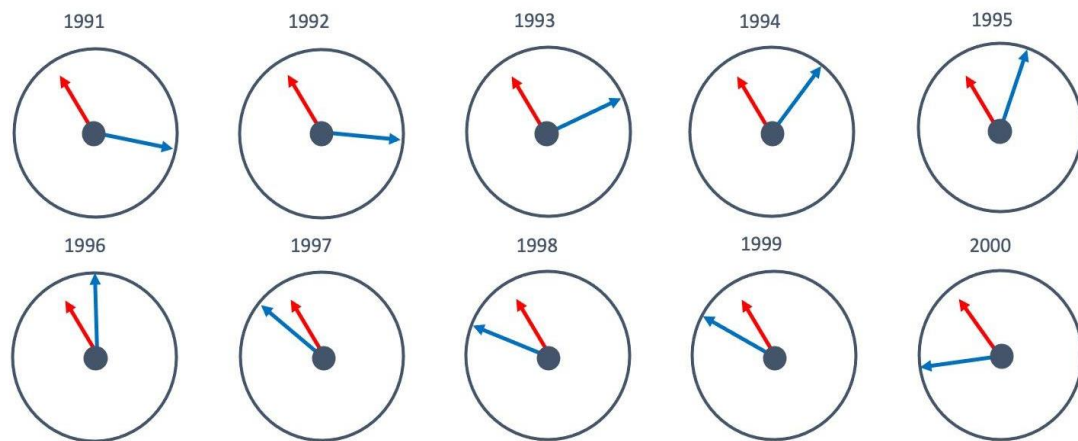


Fig. 11. Illustration of anticlockwise rotation of the velocity vector in the Subpolar East region. Anomalous geostrophic velocity (blue) and (negative) time mean temperature gradient (red). The reference level for geostrophic velocities is referenced to 1000m depth.

The anticlockwise rotation of the mean velocity vector can be seen more clearly in Fig. 11 where the velocity vector for Subtropical East (blue arrows) is normalised to 1 unit in all years. Focussing on the 1990s we see the velocity vector initially pointing south eastwards and at an obtuse angle to the mean temperature gradient (red arrow), implying a negative anomaly in the ocean heat convergence. The velocity vector tracks anticlockwise year by year until it is almost aligned with the mean temperature gradient in 1997, implying maximum ocean heat convergence in this year. In subsequent years the velocity vector continues tracking anticlockwise. In 2000, there is a near right angle between the velocity vector and the mean temperature gradient implying zero ocean heat convergence.

The decadal swings in ocean heat supply are therefore a manifestation of the rotating velocity vector periodically coming into alignment with the mean horizontal temperature gradient. The process applies at most individual locations but averaging up to the subregion scale would be affected by the spatial covariance between the horizontal velocity and the temperature gradient. In Subpolar East the spatial covariance terms are relatively small and cancel each other (Fig 7), but as mentioned earlier they are more important in the other three subregions.

The spatial correlation term involving anomalous velocity and time mean temperature gradient is significant in three of four subregions. Figure 12a shows anomalous 0-1000 m velocity vectors (blue) and time mean temperature gradient vectors (red) spatially averaged over 0-1000 m depth for the year 1990 in Subpolar West. In 1990, the contribution of the $[\overline{v}]^{**} \cdot \nabla[\overline{\theta}]^{**}$ term spatially averaged over the region was about 0 W m^{-2} and increased to

about $+20 \text{ W m}^{-2}$ over the next seven years (Fig. 8a). The magnitudes of both the anomalous velocities and the mean temperature gradient are largest in the southern part of the domain (south of $\sim 52^\circ\text{N}$) and smallest in the north. The (negative) temperature gradient is also oriented southwest in the north versus more northwest in the south. Over 1991-1997 (Fig. 12b-h), the current vectors in the north rotate clockwise, tending to bring the currents more in alignment with the temperature gradient around 1995, whereas in the south the currents rotate anticlockwise (as in the eastern domain) and are well out of alignment by 1995. The circulation regime changes from a predominantly southwards flow to a cyclonic circulation likely associated with the onset of deep convection in the Labrador Sea in the mid 1990s. The large currents to the extreme southeast do not change much until 1995 when they begin to swing anticlockwise. The systematic spatial variation of the amplitude and phase of the current with respect to the temperature gradient and their changes with time generate the time varying spatial correlation term. Similar behaviour occurs in the subtropics (not shown). Thus, the same mechanism operates in all four subregions, anomalous velocity vectors rotating in and out of alignment with the mean temperature gradient, but manifests differently where there is a large correlated spatial gradient in the magnitudes and phases of the two vectors.

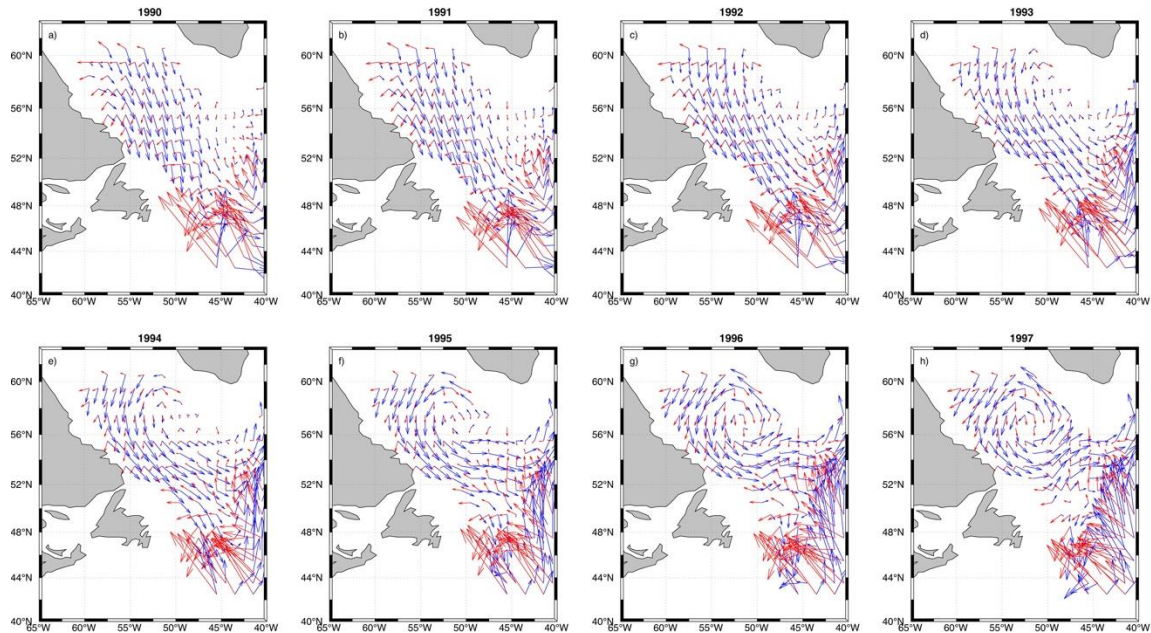


Fig. 12. Vectors of observed (EN4) decadal averaged, 0-1000m depth, anomalous geostrophic velocity (blue) and (negative) time mean temperature gradient (red) for 1990-1997, panels (a) to (h). The reference level for geostrophic velocities is referenced to 1000m depth.

h. Mechanism of decadal ocean circulation variability

The spatial average of the geostrophic current over the subregions only depends on the streamfunction along the boundaries. Thus, we hypothesize that a propagating perturbation with large horizontal length scale is responsible for the observed velocity variations. We test this hypothesis by plotting the decadal filtered geostrophic streamfunction (referenced to 1000 m depth) at four key points in the historical timeseries corresponding to the two maxima (1956, 1996) and two minima (1972, 2013) in meridional velocity. In 1956 (Fig. 13a), the streamfunction anomaly is negative at Cape Farewell ($\sim 41^\circ\text{W}$) and positive at the eastern boundary consistent with a strong positive meridional velocity. This contrasts with the situation in 1972 (Fig. 13b) when there are positive anomalies at Cape Farewell and negative anomalies at the eastern boundary, with an implied strongly negative meridional velocity. Note the thick band of negative anomalies stretching from the east coast of the USA all the way to the British Isles and Iceland. Twenty four years later in 1996 (Fig. 13c), the situation has reversed with now a stripe of positive anomalies stretching southwest to northeast, sandwiched between two areas of negative anomalies. Finally in 2013 (Fig. 13d) we have a situation reminiscent of 1972 with again a band of negative anomalies stretching from the USA to the British Isles (albeit much thinner in width), flanked by two extensive areas of positive anomalies. While these observed anomalies do not display precisely repeating patterns, the reversals on timescales of 18-20 years (hence a period of order 36-40 years) and the preferred southwest to northeast orientation are striking.

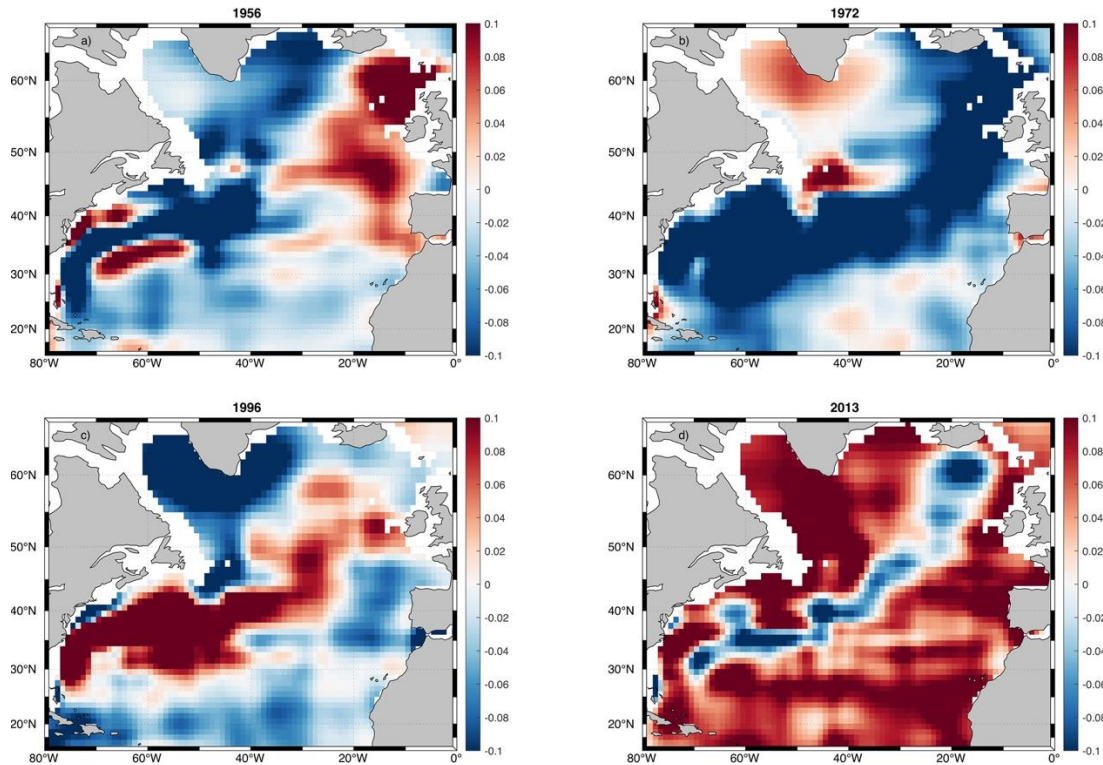


Fig. 13. Representative plots of decadal filtered geostrophic streamfunction anomaly vertically averaged over 0-1000m depth ($\text{m}^2 \text{s}^{-2}$) at key points of the multidecadal cycle (a) 1956 (b) 1972 (c) 1996 (d) 2013. The streamfunction is calculated from the EN4 gridded temperature-salinity dataset, using a fixed reference level of 1000m depth. Anomalies are calculated relative to the 1950-2020 mean. Regions with water depth less than 1000m are excluded from the analysis.

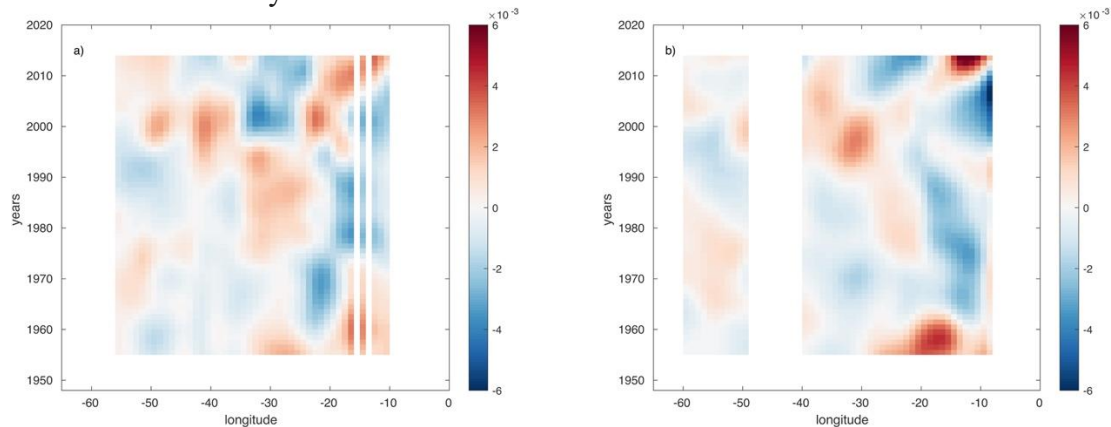


Fig. 14. Latitude-time diagram showing the 0-1000m geostrophic velocity (m s^{-1}) (component oriented southwest to northeast) at (a) 56°N (b) 61°N . The assumed level of no motion for the geostrophic calculation is 1000m.

Fig. 13 shows periodic reversals in the streamfunction patterns, but does not in itself demonstrate propagation. Figure 14 shows distance time diagrams of the 0-1000m velocity (the component oriented southwest to northeast, along the streamfunction ridges seen in Fig. 11, as we anticipate there may be propagation perpendicular to this direction. Figure 14a shows this component of velocity along the 56°N latitude line, whilst Fig 14b is along 61°N .

In Fig 14a a line of positive anomalies catches the eye, originating around 1980 at $\sim 30^\circ\text{W}$ and reaching 55°W in 2010 (propagation speed $\sim 1.6 \times 10^{-3} \text{ m s}^{-1}$). A fainter negative anomaly originates in about 1965 at $\sim 35^\circ\text{W}$ and arrives at 55°W around 1995. Anomalies with similar start and endpoints appear at 61°N (Fig 14b). The anomalies at this latitude appear to reach the east coast of Greenland ($\sim 41^\circ\text{W}$) then continue to propagate westwards from the west coast of Greenland to the east coast of North America. There is also an earlier anomaly at this latitude which originates in 1960 at 41°N on the east coast of Greenland and arrives at the North American coast ($\sim 60^\circ\text{W}$) around 1980.

This behaviour is reminiscent of a wave of pressure perturbation moving westwards, or north westwards, albeit with a very large wavelength, long period ($\sim 30\text{-}40$ years) and low frequency. A long Rossby wave has the phase speed:

$$u_\beta = \beta R_d^2, \quad (10)$$

where $\beta = \frac{\partial f}{\partial y}$ is the variation of Coriolis parameter f with latitude and R_d is the internal Rossby radius. At subpolar latitudes ($\sim 55^\circ\text{N}$), $R_d \sim 10 \text{ km}$ and $\beta = 1.3 \times 10^{-11} \text{ m}^{-1} \text{ s}^{-1}$ giving a phase speed of 0.0013 m s^{-1} . For a wavelength of $\sim 4000 \text{ km}$, the basin width at this latitude, this yields a period of 97 years, which is too slow to explain the observed timescale of variability (30-40 years).

It is well known that classical long baroclinic Rossby waves of the type seen in satellite altimetry from the 1990s onwards are about a factor of two or more faster than linear theory predicts (e.g. Chelton and Schlax, 1996, Killworth et al., 1997) Which would bring them more into line with the observed period of the variability. However satellite observations show typical wavelengths at subtropical to subpolar latitudes of a few hundred kilometres which is quite short compared to the observed length scales (Fig. 13) and modelled and observed waves travel too fast to explain the multidecadal variability we focus on here. For example, Wang et al. (2022) find combinations of β -generated and topographically generated Rossby waves take 4-10 years to cross the Atlantic basin at $\sim 60^\circ\text{N}$. Clearly, these faster propagating waves are present and do affect the variability on interannual to multiyear timescales.

Another possibility is a ‘‘thermal’’ Rossby wave (Sevellec and Federov 2013, 2015; Gastineau et al., 2018), which propagates by geostrophic self-advection along a north-south temperature gradient. The ratio of the phase speed, u_{thermal} , of a thermal Rossby wave to the

“ordinary” Rossby wave speed, u_β , is given by the following formula (derived from Sevellec and Federov, 2013), neglecting advection by mean currents (usually cancelled or exceeded by the geostrophic self-advection, the so-called “non-Doppler” effect, Sevellec and Huck, 2015):

$$u_{thermal}/u_\beta = \frac{2f}{\beta H} \frac{\partial \bar{T}/\partial y}{\partial \bar{T}/\partial z} \quad (11)$$

H is the depth of the upper layer (surface to 1000m) and $\partial \bar{T}/\partial y$, $\partial \bar{T}/\partial z$ are the mean meridional and vertical temperature gradients respectively. Typical values for the eastern subpolar gyre based on the EN4 dataset yields a thermal Rossby wave speed ~ 3 times faster than the ordinary Rossby wave ($u_{thermal} \sim 3.9 \times 10^{-3} \text{ m s}^{-1}$) and hence a period ~ 3 times smaller, bringing it into the range of 97/3 or ~ 32 years.

Consider an idealised westward propagating thermal Rossby wave, streamfunction ψ , amplitude ψ_0 :

$$\psi = \psi_0 \sin(kx + ly - \omega t) \quad (12)$$

$$\omega = \frac{-\beta^* k}{k^2 + l^2 + 1/R_d^2} \quad (13)$$

$\beta^* > \beta$ represents the effect of a north-south temperature gradient.

We initially examine the purely zonally propagating case: $k=2\pi/4000\text{km}$, $l=0$ in the subpolar east subregion (Fig. 15a). The spatial average velocity vector in the region delimited by the black box is shown in Fig. 15b. Since this wave has no meridional structure, $u=0$ identically. The spatial average velocity in the box is therefore simply the difference in the average streamfunction at the meridional boundaries of the box and the rise, fall and periodic reversal of the velocity is due to the fact that the wave has a different phase at the west of the box than at the east and the difference in the amplitude of the wave varies as it passes through the box. This simple model does not reproduce the rotation of the current vector seen in observations but reproduces the periodic phase reversals at about the right frequency. Next, we add meridional structure to the streamfunction by setting $k=2\pi/4000\text{km}$, $l=-2\pi/2000\text{km}$ (Fig. 15c), so the wave propagates to the northwest. The phase propagation of the tilted streamlines results in related changes between u and v (Fig. 15d). However, the sense of rotation is incorrect since the changes in u always precede the changes in v due to the orientation of the streamfunction isolines. To reproduce the observations, we add the two previous waves (Fig. 15e, f) and recover both the timescale and the sense of rotation of the velocity vector. Figure 15e, f seem sufficiently similar to Figs. 10, 11 and 13 that the Rossby wave mechanism seems plausible however the physical reasons behind the need for two

superimposed waves require further study. Some other features of Fig. 10 require further explanation, for example we do not fully understand the relationship between the direction of the temperature gradient and the preferred direction of the velocity vector and why the latter is different in higher versus lower latitudes (southwest to northeast in the subpolar regions and southeast to northwest in the subtropical regions). We emphasize that Fig. 15 is a kind of fitting exercise and does not in itself prove that the underlying variability is due to Rossby wave propagation, which would require further development of thermal Rossby wave theory plus a more thorough investigation of the mechanism in model simulations, however it suggests a simple and plausible explanation for the observations.

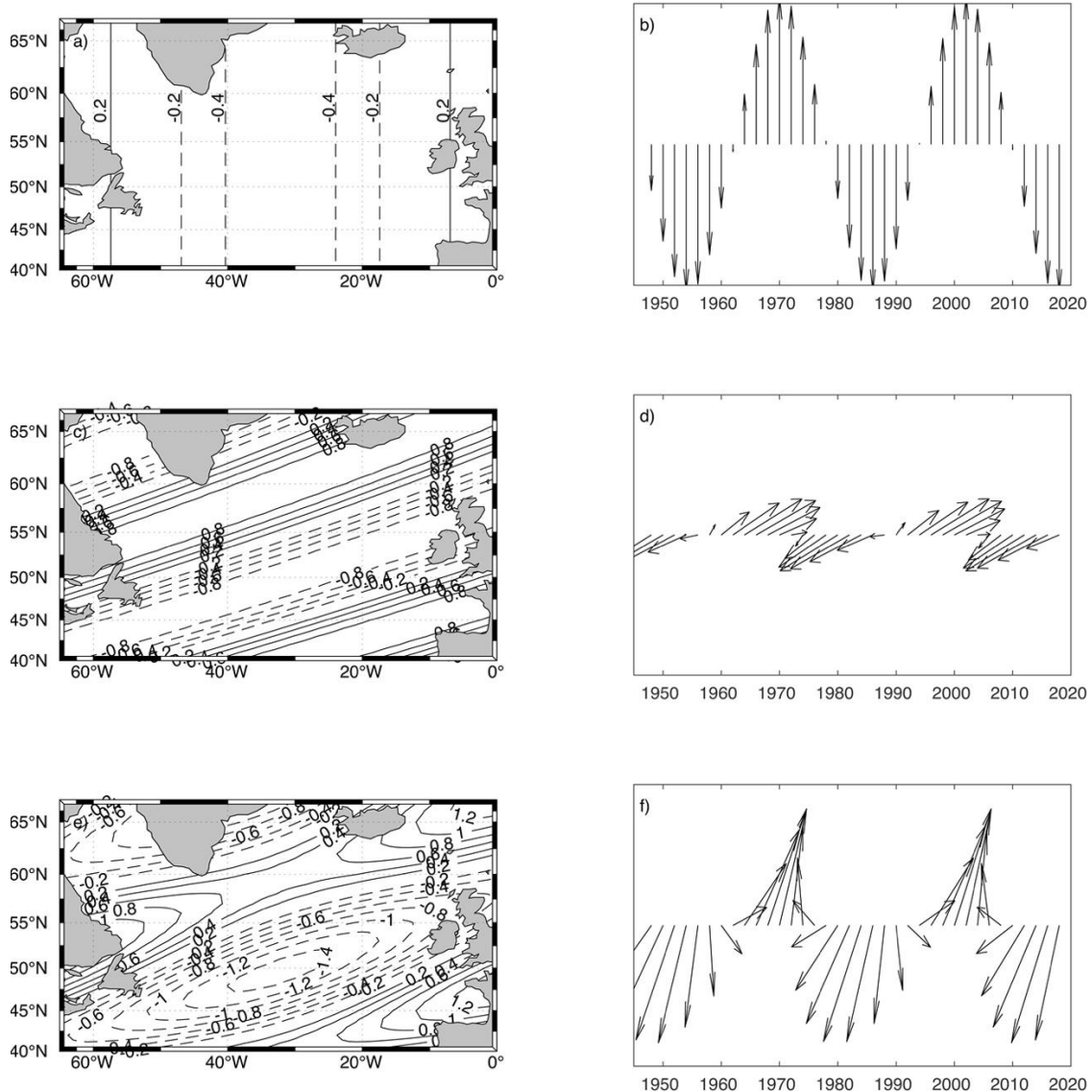


(Fig. 16a) shows negative values north of the Gulf Stream extension, around the edge of the Labrador Sea and in the central subpolar gyre, while positive correlations prevail over the Gulf Stream extension and in the central and western tropical Atlantic. A very similar (but much stronger) pattern is seen for the ocean heat supply (Fig. 16b), the main difference being over the Gulf Stream where the values are largely opposite to the OHC tendency. The surface heat flux (Fig. 16c) has an almost opposite pattern to the ocean heat supply, positive over the subpolar gyre and over the Gulf Stream extension. In the subpolar regions, ocean heat supply dominates over the surface flux forcing, whilst the situation is slightly less clear over the Gulf Stream – the surface flux seems to generally dominate the ocean heat supply and thus controls the OHC tendency there. There is thus a substantial multidecadal AMOC fingerprint in the ocean heat supply in the central subpolar gyre, with the AMOC and the ocean heat supply marching in step in the subpolar gyre. The highest correspondence with the individual budget terms are seen in a region immediately to the south east of Cape Farewell (indicated in Figures 16a-c by the solid black outline). Averages of the tendency terms in these regions are plotted alongside the AMOC index in Figure 16d to further characterize the relationship between the AMOC and the budget terms. The ocean heat supply (blue) is seen to vary in phase with the AMOC, while the surface flux term varies in antiphase.

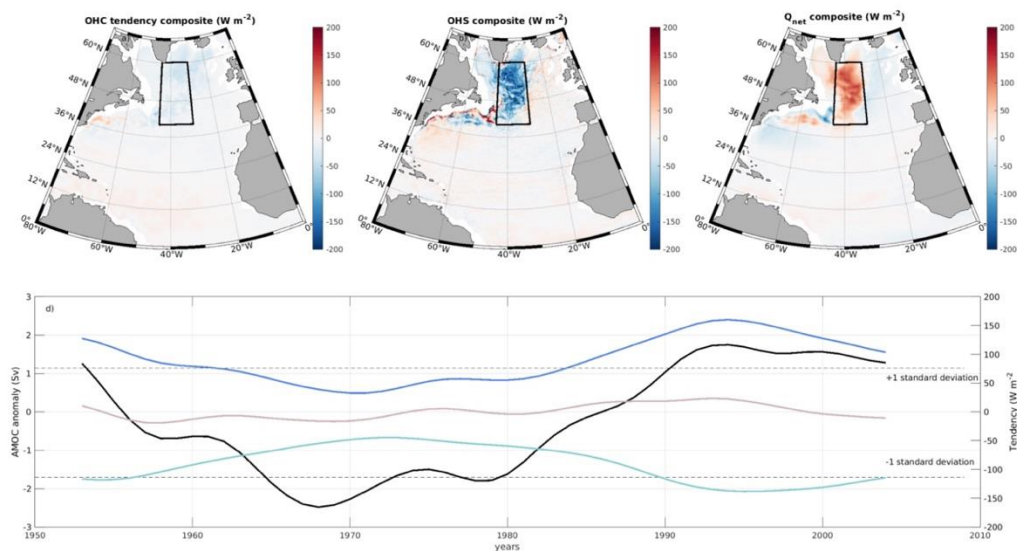


Fig. 16. (a) Difference between OHC tendencies when the decadal filtered AMOC at $26^{\circ}N$ was greater than 1 standard deviation from the mean and less than 1 standard deviation from the mean, (b) as (a) considering the ocean heat supply, (c) as (a) considering the net surface heat flux, (d) time series of decadal filtered AMOC anomaly (black) relative to the 1948-2009 mean AMOC. The average OHC (brown), OHS (blue) and the Q_{net} (green) are shown for the box indicated in the upper panels. Horizontal dotted lines show the AMOC maximum and minimum used to calculate the difference plots in panels (a), (b) and (c). All plots are based on the NEMO-CICE $1/4^{\circ}$ forced ocean simulation.

The correlations can be interpreted in conjunction with Fig. 13. Since the AMOC is a manifestation of the pressure difference across the boundary it will change in step with the progress of the thermal Rossby waves across the subpolar gyre.

The changes in the AMOC represent a change in the zonally averaged meridional velocity and as such will affect the ocean heat divergence and will be included in Fig. 10a for example. However, the lack of long term AMOC observations makes it difficult to disentangle its impact and further model analysis is required.

4. Summary and Discussion

We have constructed a three-term multidecadal upper ocean heat budget for the North Atlantic whereby ocean heat content tendency equals ocean heat supply plus surface heat flux input to determine to what extent the ocean heat supply is explained by ocean heat transport convergence. Atmospheric reanalysis products provide surface heat flux estimates whilst the ocean heat convergence is obtained using geostrophic currents and the ocean temperature gradient from gridded *in situ* ocean observations. Ocean heat content tendency is calculated from the same ocean observations. A fixed 1000m reference level is used for geostrophic calculations but we also quantify the uncertainty due to this assumption by comparing with satellite based estimates of absolute geostrophic heat convergence for the 1993-2020 period.

We demonstrate that variations in horizontal ocean heat transport divergence drive multidecadal changes in North Atlantic upper ocean heat content. In the subpolar North Atlantic, ocean heat transport divergence variations are the primary cause of such changes. Further decomposition of the ocean heat supply reveals that the dominant process is advection of the mean temperature gradient by anomalous geostrophic currents, driven by horizontal pressure gradients. In the subtropical North Atlantic, advection by geostrophic currents is important, but ageostrophic currents play an equal role. The surface heat flux remains an important contributor throughout the North Atlantic, but represents a passive feedback process.

In the subpolar gyre, we find a wavelike basin scale northwest-ward progression of geostrophic velocity anomalies. The northwest-ward progression can be modelled by a combination of two long (several thousand kilometres) wavelength propagating plane waves. The wave speed ($\sim 0.004 \text{ m s}^{-1}$) is faster than a long Rossby wave of the same wavelength and is more characteristic of a “thermal” Rossby wave driven by geostrophic self-advection due to the presence of a meridional temperature gradient. The two waves consist of one

propagating purely westward with zero meridional wavenumber and another propagating northwestward with a zonal and a meridional wavenumber.

The wavelike progression is reflected in anticlockwise rotation of the geostrophic velocity vectors throughout large parts of the North Atlantic. The explanation for observed multidecadal changes in heat content tendency is that the velocity vector periodically aligns with the mean temperature gradient. This is very marked in the eastern subpolar gyre where just two vectors, the anomalous geostrophic velocity and the mean temperature gradient determine the evolution of the heat content tendency over a very large geographical region. These two vectors are therefore potentially a very useful predictor of near-term changes to the ocean heat content and SST in the subpolar gyre. In the western subpolar gyre, large correlated spatial variations in both temperature gradient and the magnitude and phase of the anomalous velocity make predictions more difficult, but nonetheless the anomalous velocity linked to the wave propagation determines the heat content tendency to a large extent. In the subtropics more processes are involved including ageostrophic advection of heat, advection of temperature anomalies by the mean current and the impact of vertical structure.

The trigger for the subpolar variability remains a big question. If a damped thermal Rossby wave is the explanation for the variability then there would need to be some mechanism to excite this – for example random atmospheric weather variability, mesoscale eddies or perhaps boundary wave propagation (Gastineau et al., 2018). It remains unclear why there would be two waves excited and what sets the amplitude of the variability. There is however also the possibility that the Rossby wave represents an unstable mode, a consequence of generalized baroclinic instability (Sevellec and Huck, 2015). In this situation the waves could be self sustaining. Further investigation is required to discriminate between the two possibilities.

We find a good correspondence between ocean heat supply and the AMOC especially in the subpolar gyre, however it remains unclear how much the AMOC anomalies are a cause rather than an effect of the wave propagation in the gyre. Nonetheless, the AMOC remains an excellent predictor of the subpolar gyre heat content and vice versa.

The eastern subpolar region emerges as the most predictable region and there are interesting implications for climate change projections. Any changes which impact the horizontal temperature gradient could affect both the amplitude and timescale of decadal variability in the SPG for example.

A novel aspect is the combination of the model and the observation-based heat budget to constrain the geostrophic reference level. We conclude that 1000 m is a realistic choice for reference level in the eastern North Atlantic (compare with e.g. Stramma, 1984, who used classical hydrographic methods to deduce reference levels of 1200-1500 m in the eastern subtropics) and varies little on multidecadal timescales. In the western subpolar region and the subtropics the level of no motion varies considerably on decadal and possibly longer timescales, suggesting that the barotropic component is changing, although the reason for this is as yet unclear.

Topics for future investigation include the impact of the mean North Atlantic current, the lag between subpolar and subtropical variability, and the origin of the ageostrophic currents in the subtropical gyre.

An important follow up would be to understand how well climate models reproduce the observed behaviour. The wave propagation process encodes substantial predictability into the system and offer the possibility of understanding barriers to predictability, of discriminating between models and is a potentially very powerful emergent constraint on climate model projections.

Finally, understanding the relationship between upper ocean heat content and sea-surface temperature on decadal timescales remains an important and challenging topic. Future work should include finding methods to extend previous interannual timescale studies of the mixed layer heat budget (Buckley et al., 2014, Roberts et al., 2017, Josey and Sinha, 2022) to decadal timescales.

Acknowledgments.

This research was supported by the NERC Atlantic Climate System Integrated Study (ACSIS) Programme (NE/N018044/1); the NERC Wider Impacts of Subpolar North Atlantic decadal variability on the Ocean and atmosphere (WISHBONE) project (NE/T013540/1); the NERC Climate Change in the Arctic-North Atlantic region and impacts on the UK (CANARI) Programme; CLASS (NE/R015953/1) and the NERC funded RAPID AMOC programme at 26°N. This research has received funding from the European Union's Horizon 2020 research and innovation programme under grant agreement No 820989 (COMFORT). The work reflects only the authors' view; the European Commission and their executive agency are not responsible for any use that may be made of the information the work

contains. We acknowledge useful discussions with Joel Hirschi, David Smeed, Thierry Penduff, Kristofer Doos and Florian Sévellec.

Data Availability Statement.

All observational datasets used in this study are in the public domain (see references in Section 2a) as is the NEMO GO6 model configuration.

REFERENCES

- Booth, B. B., N. J. Dunstone, P. R. Halloran, T. Andrews, and N. Bellouin, 2012: Aerosols implicated as a prime driver of twentieth-century North Atlantic climate variability. *Nature*, **484**, 228–232, <https://doi.org/10.1038/nature10946>.
- Buckley, M. W., R. M. Ponte, G. Forget, and P. Heimbach, 2014: Low-frequency SST and upper-ocean heat content variability in the North Atlantic. *J. Climate*, **27**, 4996–5018, <https://doi.org/10.1175/JCLI-D-13-00316.1>.
- Buckley, M. W., and J. Marshall, 2016: Observations, inferences, and mechanisms of the Atlantic Meridional Overturning Circulation: A review, *Rev. of Geophysics*. 54, 5-63, <https://doi.org/10.1002/2015RG000493>
- Chelton D. B. and M. G. Schlax. 1996: Global observations of oceanic Rossby Waves. *Science*, 272, 234-238. Doi: DOI: 10.1126/science.272.5259.234
- Clement, A., K. Bellomo, L. N. Murphy, M. A. Cane, T. Mauritsen, G. Rädel, and B. Stevens, 2015: The Atlantic multidecadal oscillation without a role for ocean circulation. *Science*, **350**, 320–324, <https://doi.org/10.1126/science.aab3980>.
- Copernicus Climate Change Service, Climate Data Store, (2018): Sea level gridded data from satellite observations for the global ocean from 1993 to present. Copernicus Climate Change Service (C3S) Climate Data Store (CDS). DOI: 10.24381/cds.4c328c78 (Accessed on 10-10-2023)
- Desbruyères, D. G., B. Sinha, E. L. McDonagh, S. A. Josey, N. P. Holliday N.P., D. A. Smeed, A. L. New, A. Megann, and B. I. Moat, 2020: Importance of boundary processes for heat uptake in the subpolar north Atlantic. *J. Geophys. Res. Oceans*, **125**, 1-16, <https://doi.org/10.1029/2020JC016366>.

- Drews, A., and R. J. Greatbatch, 2017: Evolution of the Atlantic multidecadal variability in a model with an improved North Atlantic Current. *J. Climate*, **30**, 5491-5512, <https://doi.org/10.1175/JCLI-D-16-0790.1>.
- Emery, W. J., and R. E. Thomson, 1997: *Data Analysis Methods in Physical Oceanography*. Pergamon, 634 pp.
- Enfield, D. B., A. M. Mestas-Nuñez, and P. J. Trimble, 2001: The Atlantic multidecadal oscillation and its relation to rainfall and river flows in the continental U.S. *Geophys. Res. Lett.*, **28**, 2077–2080, <https://doi.org/10.1029/2000GL012745>.
- Gastineau, G., and C. Frankignoul, 2015: Influence of the North Atlantic SST variability on the atmospheric circulation during the twentieth century. *Journal of Climate*, **28**, 1396–1416. <https://doi.org/10.1175/JCLI-D-14-00424.1>.
- Gastineau, G., J. Mignot, O. Arzel, and T. Huck, 2018: North Atlantic Ocean internal decadal variability: Role of the mean state and ocean–atmosphere coupling. *J. Geophys. Res. Oceans*, **123**, 5949–5970, <https://doi.org/10.1029/2018JC014074>.
- Good, S. A., M. J. Martin and N. A. Rayner, 2013: EN4 quality controlled ocean temperature and salinity profiles and monthly objective analyses with uncertainty estimates. *Journal of Geophysical Research: Oceans*, **118**, 6704-6716, doi:10.1002/2013JC009067.
- Griffies, S. M., and coauthors, 2016: OMIP contribution to CMIP6: experimental and diagnostic protocol for the physical component of the Ocean Model Intercomparison Project, *Geosci. Model Dev.*, **9**, 3231–3296, <https://doi.org/10.5194/gmd-9-3231-2016>.
- Hersbach H & coauthors, 2020: The ERA5 Global Reanalysis. *Q. J. Roy Meteorol. Soc.*, **146**, 1999-2049. <https://doi.org/10.1002/qj3803>.
- Hirschi, J. J.-M. and coauthors, 2020: The Atlantic meridional overturning circulation in high resolution models. *J. of Geo. Res. Oceans*, 125 (4), e2019JC015522. <https://doi.org/10.1029/2019JC015522>
- Hunke, E. C. and J. K. Dukowicz, 1997: An Elastic–Viscous–Plastic Model for Sea Ice Dynamics. *J. Phys. Oceanogr.*, **27**, 1849–1867, [https://doi.org/10.1175/1520-0485\(1997\)027<1849:AEVPMF>2.0.CO;2](https://doi.org/10.1175/1520-0485(1997)027<1849:AEVPMF>2.0.CO;2).
- Josey, S. A., and B. Sinha, 2022: Subpolar Atlantic Ocean mixed layer heat content variability is increasingly driven by an active ocean. *Communications Earth & Environment*, **3**, <https://doi.org/10.1038/s43247-022-00433-6>.

- Killworth, P. D., Chelton, D. B., & De Szoeke, R. A. (1997). The speed of observed and theoretical long extratropical planetary waves. *Journal of Physical Oceanography*. [https://doi.org/10.1175/1520-0485\(1997\)027<1946:tsooat>2.0.co;2](https://doi.org/10.1175/1520-0485(1997)027<1946:tsooat>2.0.co;2)
- Knight, J. R., C. K. Folland, and A. A. Scaife, 2006: Climate impacts of the Atlantic multidecadal oscillation. *Geophys. Res. Lett.*, **33**, L17706, <https://doi.org/10.1029/2006GL026242>.
- Kushnir, Y., 1994: Interdecadal variations in North Atlantic sea-surface temperature and associated atmospheric conditions. *J. Clim.*, **7**, 141– 157.
- Lai, W. K. M., J. I. Robson, L. J. Wilcox, and N. Dunstone, 2022: Mechanisms of Internal Atlantic Multidecadal Variability in HadGEM3-GC3.1 at Two Different Resolutions. *J. Climate*, **35**, 1365–1383, <https://doi.org/10.1175/JCLI-D-21-0281.1>.
- McCarthy, G. D., I. D. Haigh, J. J.-M., Hirschi, J. P. Grist, D. A. Smeed, 2015: Ocean impact on decadal Atlantic climate variability revealed by sea-level observations. *Nature*, **521** (7553). 508-510. <https://doi.org/10.1038/nature14491>.
- Madec, G, and Coauthors, 2016: *NEMO ocean engine*. Note du Pole de modelisation de l’Institut Pierre-Simon Laplace No 27, ISSN No 1288-1619.
- Menary M. B., D. L. R. Hodson , J. I. Robson , R. T. Sutton , and R. A. Wood, 2015: A Mechanism of Internal Decadal Atlantic Ocean Variability in a High-Resolution Coupled Climate Model. *Journal of Climate*, **28**, 7764–7785, <https://doi.org/10.1175/JCLI-D-15-0106.1>
- Moat, B. I, B. Sinha, S. A. Josey, J. Robson, P. Ortega, F. Sévellec, N. P. Holliday, G. D. McCarthy, A. L. New, and J. J.-M. Hirschi, 2019: Insights into decadal North Atlantic sea-surface temperature and ocean heat content variability from an eddy-permitting coupled climate model. *Journal of Climate*, **32**, 6137-6161. <https://doi.org/10.1175/JCLI-D-18-0709.1> .
- Moat B. I., B. A. King, and C. R. Macintosh C.R., 2021: Subpolar North Atlantic ocean heat content (surface to 1000m) using objectively mapped Argo profiling float data. NERC EDS British Oceanographic Data Centre NOC, doi:10.5285/d23c26bc-6e6c-5bbf-e053-6c86abc02cfb.

- Msadek, R., and C. Frankignoul, 2009: Atlantic multidecadal oceanic variability and its influence on the atmosphere in a climate model. *Climate Dyn.*, **33**, 45–62, <https://doi.org/10.1007/s00382-008-0452-0>.
- Muir, L. C., and A. V. Fedorov, 2017: Evidence of the AMOC interdecadal mode related to westward propagation of temperature anomalies in CMIP5 models. *Climate Dynamics*, **48**, 1517–1535. <https://doi.org/10.1007/s00382-016-3157-9>.
- Otterå, O. H., M. Bentsen, H. Drange, and L. Suo, 2010: External forcing as a metronome for Atlantic multidecadal variability. *Nat. Geosci.*, **3**, 688–694, <https://doi.org/10.1038/ngeo955>.
- Pond, S and G. L. Pickard, 1983: *Introductory Dynamical Oceanography 2nd Edition*, Butterworth-Heinemann, 329pp.
- Roberts, C. D., M. D. Palmer, R. P. Allan, D. G. Desbruyères, P. Hyder, C. Liu, and D. Smith, 2017: Surface flux and ocean heat transport convergence contributions to seasonal and interannual variations of ocean heat content. *J. Geophys. Res. Oceans*, **122**, 726–744, <https://doi.org/10.1002/2016JC012278>.
- Robson, J., R. T. Sutton, and D. M. Smith, 2012: Initialized decadal predictions of the rapid warming of the North Atlantic Ocean in the mid 1990s. *Geophys. Res. Lett.*, **39**, L19713, <https://doi.org/10.1029/2012GL053370>.
- Robson, J., P. Ortega, and R. T. Sutton, 2016: A reversal of climatic trends in the North Atlantic since 2005. *Nat. Geosci.*, **9**, 513–517, <https://doi.org/10.1038/ngeo2727>.
- Robson, J. and Coauthors, 2018: Recent multivariate changes in the North Atlantic climate system, with a focus on 2005–2016. *International Journal of Climatology*, **38**, 5050–5076. <https://doi.org/10.1002/joc.5815>.
- Robson, J., M. B. Menary, R. T. Sutton, J. Mecking, J. M. Gregory, C. Jones, B. Sinha, D. P. Stevens, and L. J. Wilcox, 2022: The role of anthropogenic aerosol forcing in the 1850–1985 strengthening of the AMOC in CMIP6 historical simulations. *Journal of Climate*, **35**, 3243–3263. <https://doi.org/10.1175/JCLI-D-22-0124.1>.
- Scaife, A.A., L. Hermanson, A. van Niekerk, and Coauthors, 2022: Long-range predictability of extratropical climate and the length of day. *Nat. Geosci.* **15**, 789–793, <https://doi.org/10.1038/s41561-022-01037-7>.

- Sévellec, F., and A. V. Fedorov, 2013: The leading, interdecadal eigenmode of the Atlantic Meridional Overturning Circulation in a realistic ocean model. *Journal of Climate*, **26**, 2160–2183, <https://doi.org/10.1175/JCLI-D-11-00023.1>.
- Sévellec F., and T. Huck, 2015: Theoretical Investigation of the Atlantic Multidecadal Oscillation. *J. Phys. Oceanogr.*, **45**, 2189–2208, <https://doi.org/10.1175/JPO-D-14-0094>.
- Sévellec F., and A. V. Fedorov, 2015: Optimal excitation of AMOC decadal variability: links to the subpolar ocean. *Prog. Oceanogr.*, **132**, 287–304, <https://doi.org/10.1016/j.pocean.2014.02.006>.
- Sévellec, F., and B. Sinha, 2018: Predictability of decadal Atlantic meridional overturning circulation variations. *Oxford Research Encyclopaedias: Climate Science*, <https://doi.org/10.1093/acrefore/9780190228620.013.81>.
- Smith, D. M., and J. M. Murphy, 2007: An objective ocean temperature and salinity analysis using covariances from a global climate model. *J. Geophys. Res.*, **112**, C02022, <https://doi.org/10.1029/2005JC003172>.
- Smith, D. M., R. P. Allan, A. C. Coward, R. Eade, P. Hyder, C. Liu, N. G. Loeb, M. D. Palmer, C. D. Roberts, and A. A. Scaife, 2015: Earth's energy imbalance since 1960 in observations and CMIP5 models. *Geophys. Res. Lett.* **42**, 1205–13, <https://doi.org/10.1002/2014GL062669>.
- Storkey, D., A. Blaker, P. Mathiot, A. Megann, Y. Aksenov, E. W. Blockley, D. Calvert, T. Graham, H. T. Hewitt, P. Hyder, T. Kuhlbrodt, J. G. L. Rae, and B. Sinha, 2018: UK Global Ocean GO6 and GO7: a traceable hierarchy of model resolutions. *Geoscientific Model Development*, **11**, 3187–3213, <https://doi.org/10.5194/gmd-11-3187-2018>.
- Stramma, L., 1984; Geostrophic transport in the Warm Water Sphere of the eastern subtropical North Atlantic. *Journal of Marine Research*, **42**, 537–558, <https://doi.org/10.1357/002224084788506022>
- Sutton, R. T., and B. Dong, 2012: Atlantic Ocean influence on a shift in European climate in the 1990s. *Nat. Geosci.*, **5**, 788–792, <https://doi.org/10.1038/ngeo1595>.
- Sutton, R.T., G. D. McCarthy, J. Robson, B. Sinha, A. Archibald, L. J. Gray, 2018: Atlantic multi-decadal variability and the UK ACSIS programme. *Bulletin of the American Meteorological Society*, <https://doi.org/10.1175/BAMS-D-16-0266.1>.

- Swingedouw, D., P. Ortega, J. Mignot, E. Guilyardi, V. Masson-Delmotte, P. G. Butler, M. Khodri, and R. Séférian, 2015: Bidecadal North Atlantic ocean circulation variability controlled by timing of volcanic eruptions. *Nat. Commun.*, **6**, 6545, <https://doi.org/10.1038/ncomms7545>.
- Tsujino H., and coauthors, 2020: Evaluation of global ocean–sea-ice model simulations based on the experimental protocols of the Ocean Model Intercomparison Project phase 2 (OMIP-2). *Geoscientific Model Development*, **13**, 3643–3708, <https://doi.org/10.5194/gmd-13-3643-2020>.
- Wang, H., Li Ziguang, Xiaopel Lin, Jian Zhao and Dexing Wu, (2022): Adiabatic Processes Contribute to the Rapid Warming of Subpolar North Atlantic During 1993-2010, *J. of Geo. Res. Oceans*, **127**(4): e2021JC018234. <https://doi.org/10.1029/2021JC018234>
- World Climate Research Programme, 2023a: Explaining and Predicting Earth System Change. <https://www.wcrp-climate.org/epesc>.
- World Climate Research Programme, 2023b: Grand Challenge on Near-Term Climate Prediction. <https://www.wcrp-climate.org/gc-near-term-climate-prediction>.
- Yeager, S. G. and J. I. Robson, 2017: Recent progress in understanding and predicting Atlantic Decadal Climate Variability. *Curr. Clim. Change. Rep.*, **3**, 112–127, <https://doi.org/10.1007/s40641-017-0064-z>.
- Zhang, R., 2008: Coherent surface–subsurface fingerprint of the Atlantic meridional overturning circulation. *Geophys. Res. Lett.*, **35**, L20705, <https://doi.org/10.1029/2008GL035463>.
- Zhang, J., and R. Zhang, 2015: On the evolution of Atlantic meridional overturning circulation fingerprint and implications for decadal predictability in the North Atlantic. *Geophys. Res. Lett.* **35**, 5419–5426, <https://doi.org/10.1002/2015GL064596>.
- Zhang, R., R. Sutton, G. Danabasoglu, and Coauthors, 2019: A review of the role of the Atlantic Meridional Overturning Circulation in Atlantic Multidecadal Variability and associated climate impacts. *Rev. Geophys.*, **57**, 316–375.